DESIGN AND SYNTHESIS OF HARMONIC SURFACE ACOUSTIC WAVE DELAY LINES

By

PATRICK M. NARAINE(B.Eng.)

A Thesis

Submitted to the School of Graduate Studies

in Partial Fulfilment of the Requirements

for the Degree

Master of Engineering

McMaster University
Hamilton, Ontario

September 1980

MASTER OF ENGINEERING(1980) McMaster University
(Electrical Engineering) Hamilton, Ontario.

TITLE: Design and Synthesis of Harmonic Surface Acoustic Wave Delay Lines.

AUTHOR: Patrick M. Naraine, B.Eng. (McMaster University)

SUPERVISOR: Professor C. K. Campbell

NUMBER OF PAGES: (xi), 114.

SCOPE AND CONTENTS:

The design and synthesis of Surface Acoustic Wave delay lines operating at a higher harmonic mode.

ABSTRACT

Harmonic delay lines are necessary for building SAW oscillators in the 200 MHz - 1 GHz frequency range using conventional photolithographic techniques. The various methods of generating and filtering higher harmonic modes in Surface Acoustic Wave (SAW) delay lines are presented in this thesis. A new design called the "stepped-finger" design, for SAW transducers was also developed in this thesis. A stepped-finger harmonic delay line was built, tested and compared with the only other presently existing harmonic delay line structure, the 3- and 4-finger delay line. The experimental results obtained indicated that the stepped-finger delay line was the more efficient of the two.

ACKNOWLEDGEMENTS

I would like to thank Dr. C. K. Campbell for sharing with me his invaluable experience and knowledge of SAW devices, and for his supervision and encouragement throughout the course of this project.

Thanks are also due to Mr. Yanglin Ye for his assistance in the fabrication of the delay lines and for his numerous suggestions and advice.

Mr. Joe Sferrazza also deserves thanks for his input to our many stimulating discussions.

I would like to express my appreciation to Mr. Mark Usik for maintaining and repairing the equipment used in these experiments.

Finally, thanks to C. McAloney for typing and proofreading this thesis.

TABLE OF CONTENTS

LIST OF FIGURES

CHAPTER I

INTRODUCTION

1.1 Operating Principles of Surface Acoustic Waves

Any unbounded solid can propagate and support a mode of elastic (mechanical) waves. These waves carry vibrational energy parallel to the surface of the solid and are called Surface Acoustic Waves (SAW's). Generally, the usable frequency range of these waves are in the mega- to gigahertz range.

The elastic waves of particular importance are called Rayleigh waves. The velocity of these waves are constant for a particular crystal and lie in the range of 1,000 to 6,000 m/sec. This slow velocity of the surface acoustic wave relative to that of electromagnetic waves results in a spatial compression of a signal by about 10^5 along the propagation path. For example a 3μs long signal will occupy 1 km as an electromagnetic wave, but only 1 cm as a surface acoustic wave. SAW's propagate close to the surface of the solid, so that the mechanical energy carried by these waves is largest on the surface. If the solid is of piezoelectric material, the waves travelling on its surface will

induce local electric fields. These electric fields will extend above the surface of the piezoelectric solid and will propagate along with the mechanical surface waves.

The surface acoustic wave can be launched from an electrical signal, processed and reconverted back to an electrical signal, by using Interdigital Transducers (IDT's) as shown in Figure 1.1. The IDT consists of thin conducting strips (fingers) deposited onto the surface of the piezoelectric substrate. Adjacent strips in each transducer are connected to alternate bus bars, so that the polarity of each finger alternates in a sequential manner. The repeat distance (periodicity), 2L, is made equal to the wavelength, λ_o, corresponding to the centre frequency, f_o, the frequency at which maximum response occurs, i.e.:

$$f_o = \frac{v}{\lambda_o} = \frac{v}{2L} \tag{1.1}$$

where v is the velocity of the SAW.

The input transducer launches both a forward wave (towards the output transducer) and a backward wave. The unwanted backward wave is eliminated by an acoustic absorber so that it will not be reflected from the end of the crystal and interfere with the forward wave. By reciprocity, the output transducer is also bidirectional and some of the incident acoustic wave passes under the transducer and must be absorbed at the end of the crystal.

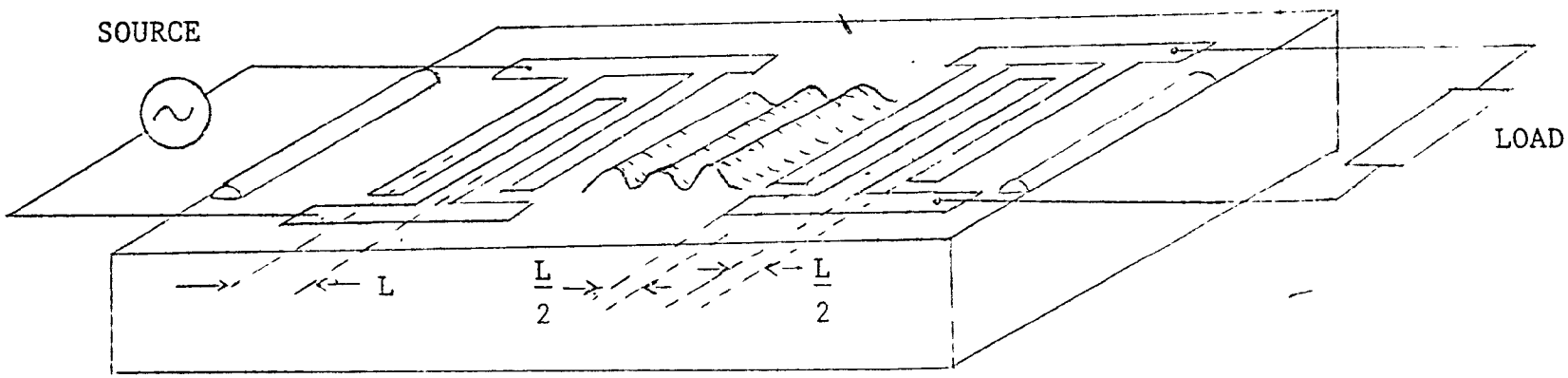

Fig. 1.1 Transmitting and Receiving Interdigital Transducers on the surface of a piezoelectric substrate.

In SAW devices there is a direct relationship between the transducer geometry and its impulse response, h(t). The impulse response is related to the frequency response by the Fourier transform.

$$h(t) = \int_{-\infty}^{\infty} H(f) \exp(j2\pi ft)\, df \tag{1.2}$$

Thus by controlling the finger positions and the extent of overlap between adjacent fingers, the impulse response and frequency response may be tailored to any desired specification. The most commonly used geometric structures in SAW devices and the resulting impulse and frequency responses are shown in Figure 1.2. Note the correspondence between transducer structure and impulse response. Note also that the frequency response in Figure 1.2(b) is not idealy rectangular, but contains ripples in the pass band and stop band due to the truncation of the sinc function in the transducer geometry.

SAW devices generally consist of a transmitting (input) IDT, with frequency response $H_{in}(f)$, and a receiving (output) IDT, with frequency response $H_{out}(f)$. So the overall frequency response of the device will be the product of the two responses modified by a delay factor, i.e.:

$$H_T(f) = H_{in}(f) \cdot H_{out}(f) \cdot \exp(-j2\pi fT) \tag{1.3}$$

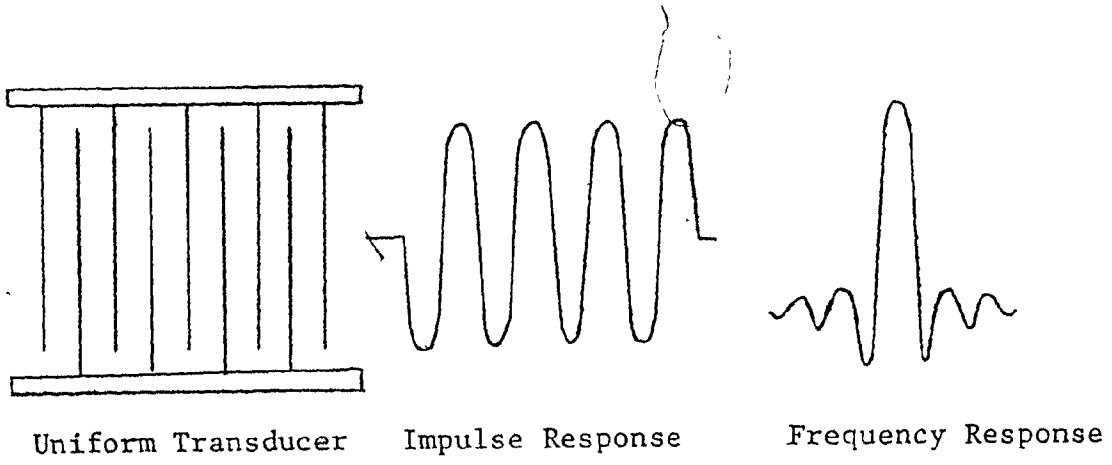

Fig. 1.2 The most commonly used geometric structures in SAW devices and the resulting impulse and frequency responses.

In designing a SAW device consideration must also be given to second order effects such as:

(1) Triple transit echoes.

(2) Wave reflection at finger edges.

(3) Nonplanar wavefronts.

(4) Diffraction and beam steering.

(5) Spurious acoustic modes (Bulk and plate waves).

(6) Electromagnetic feedthrough.

(7) Electrode resistivity.

(8) Electrode mass loading.

Methods of reducing these second order effects are discussed in detail in [1].

1.2 Scope of This Thesis

Because of their advantages of small size, light weight, ruggedness and planar structures which rely on a technology similar to that employed in the fabrication of integrated circuits, SAW devices are being used in increasing number for military and commercial signal-processing systems. However, there are still many problems encountered in the fabrication of SAW devices. One of these problems is the production of SAW devices that are capable of operating in the 200 MHz - 1 GHz frequency range.

SAW devices can be made with fundamental frequencies below 200 MHz using photolithographic techniques. On a contract for CRC, Campbell [9] was able to successfully

build a SAW delay line operating at a fundamental frequency of 183 MHz, using the photolithographic equipment of the SAW device fabrication laboratory at McMaster University. This upper frequency limit was set according to the resolution of the existing photoreduction lens (200 line pair/mm), and the resolution limitations in the photoresist processes.

Later Campbell and Seiler [29] built SAW delay lines at fundamental frequencies of 1 GHz and 2 GHz using a scanning electron microscope (SEM) modified for electron-beam lithography. Here the lower frequency limit was set according to the existing field of view of the SEM.

The solution to the problem of operating a SAW device in the 200 MHz - 1 GHz range, is to simply make the device with a fundamental frequency below 200 MHz using normal photolithographic techniques, and to operate the device at a higher harmonic frequency which is in the 200 MHz - 1 GHz frequency range. However, another problem arises, that of efficiently generating the higher harmonic mode and the filtering of this mode from the undesired other harmonics which are inevitably simultaneously generated. The solution to this problem is the primary purpose for this thesis.

The most accurate circuit model available for describing SAW transducers operating at higher harmonic modes is identified and described in Chapter II.

Chapter III deals with the problems encountered with higher harmonic mode operation of SAW devices.

Solutions to these problems are outlined in Chapter IV. In this chapter the only existing solution previous to this thesis, which was developed by Kerbel [11] and Engan [15] is outlined. The author's solution, which makes use of a new transducer design called the "stepped-finger" transducer, is also stated.

Two delay lines, one using Kerbel's and Engan's method and the other using the author's stepped-finger method, were designed and fabricated as presented in Chapter V.

The experimental results obtained from the two delay lines are presented in Chapter VI.

Finally in Chapter VII comparisons are made between the two delay lines to ascertain which of the two methods is the more efficient.

CHAPTER II

HARMONIC-FREQUENCY CIRCUIT-MODELS

2.1 General

Representing SAW interdigital transducers by a simple model is the most efficient way of determining the transfer matrices of the input and output transducer. This then allows the amplitude and phase response of the SAW device to be determined as a function of frequency. Second order effects such as reflections from input and output transducers, device mismatching, etc., can be included in the model.

Since the advent of SAW devices numerous models have been proposed. A summary of the most used models and their capabilities is given in Figure 2.1 [2].

The delta function model was introduced by Tancrell and Holland [3]. This model gives a good description of the bandshape near the fundamental frequency, but incurs severe errors far from the fundamental frequency and thus fails to predict the correct levels of the harmonic responses.

The spatial harmonic model was first derived for an infinite periodic "single-electrode" transducer in the

CAPABILITIES	MODEL				
	DELTA FUNCTION MODEL	SPATIAL HARMONIC ANALYSIS	IMPULSE MODEL	CROSSED FIELD MODEL	GENERALIZED CIRCUIT MODEL
TRANSDUCER DESIGN PRESCRIPTION	√		√	√	(**)
ELECTRIC IMPEDANCE			√ (*)	√	√
MATCHING CIRCUIT EASILY INCLUDED			√ (*)	√	√
OVERTONE OPERATION AND ARBITRARY METALLIZATION RATIO		√			√
DETAILED SIMULATION 2-TRANSDUCER FILTER WITH MATCHING CKTS., ELECTRODE LOADING, TRIPLE TRANSIT ECHOES				√	√
BULK WAVES					

(*) APPEALS TO CROSSED FIELD MODEL FOR PIEZOELECTRIC COUPLING STRENGTH
(**) GENERATES DESCRIPTIONS AS WITH CROSSED FIELD MODEL; NOT PRESENTLY GENERALIZED TO CORRECT FOR HARMONIC OPERATION AND ARBITRARY METALLIZATION RATIOS

Fig 2.1 Summary of the most commonly used SAW models and their capabilities. [2]

important early work by Engan [4]. This was the first time a model was derived to explain harmonic operations in SAW devices. The model accurately predicts the relative harmonic amplitudes, but makes the assumptions of small piezoelectric coupling and a sufficiently long transducer so that end effects could be neglected.

Both the impulse model of Hartmann et. al., [5] and the crossed field Mason circuit model [6] are rather accurate for describing the IDT operation in the fundamental pass band. The crossed field model has the added advantage of describing transducers containing externally matched circuits, electrode loading and triple transit echoes. However, both models, like the delta function model, are inaccurate when used to describe overtone operations.

The generalized circuit model developed by Smith et. al., [7] of Hughes Aircraft Company is the most accurate model developed to date for the characterization of both fundamental and higher harmonic operation. The model is capable of describing transducers containing any number of fingers, in any polarity sequence, and with arbitrary metallization ratio. This model was adopted in this thesis for the generation of higher harmonic modes, and so it is described in detail in the next section.

2.2 The Generalized Circuit Model

A SAW transducer consists of two acoustic ports and one electrical port. Thus a three port network, as shown in Figure 2.2, would be sufficient for describing all the transfer functions of the transducer. In Figure 2.2 ports 1 and 2 are the acoustic ports. The "voltages" E_1, and E_2 and the "currents" I_1 and I_2 are representative of the acoustic wave forces and acoustic wave velocities respectively. Port 3 is the electric port, with the voltage E_3 and current I_3 representing the actual voltage and current applied to the bus bars of the transducer The currents and voltages of the three port network are related by the admittance matrix Y_{ij}, i.e.:

$$I_i = \sum_{j=1}^{3} Y_{ij} E_j \quad , \; i=1, 2, 3 \tag{2.1}$$

The generalized circuit model uses the Krimholtz circuit [8] to represent an electrode and gap region, as shown in Figure 2.3. N number of these circuits are then connected together, as shown in Figure 2.4, to represent a transducer consisting of N electrodes and gaps. Thus by finding the y_{ij} of all electrodes, the admittance matrix Y_{ij} of the entire transducer can be found.

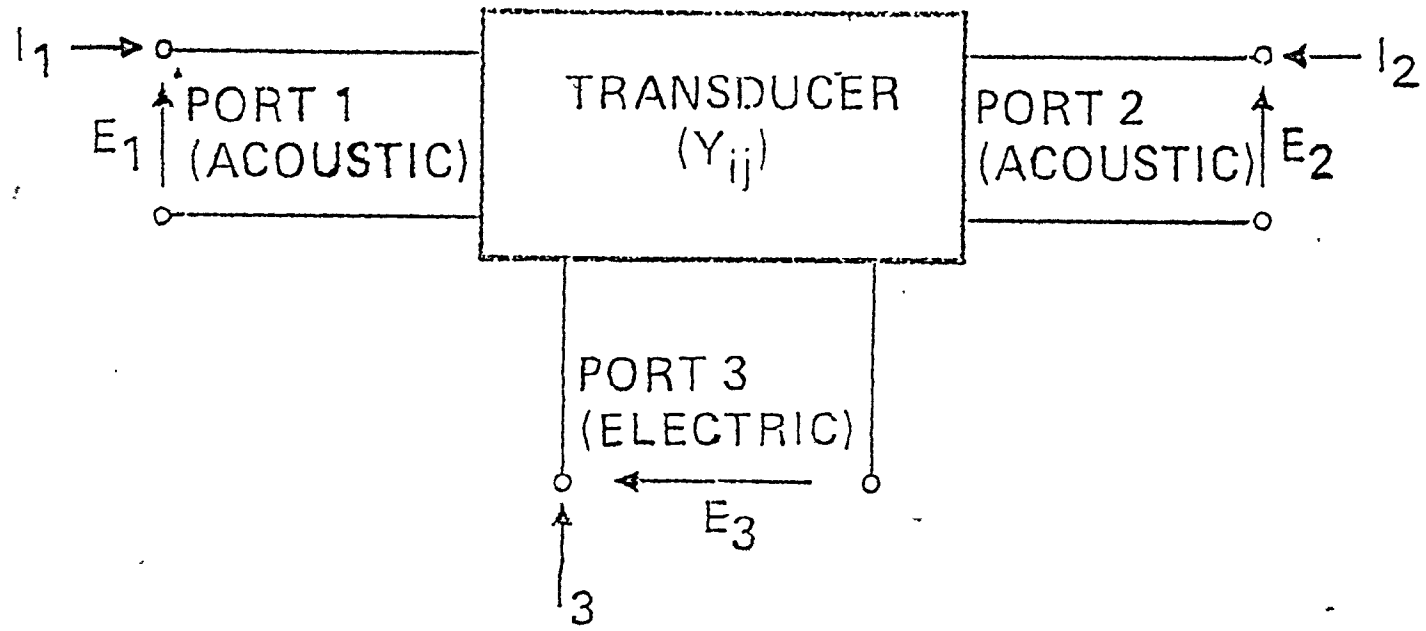

$$I_j = \sum_{j=1}^{3} Y_{ij} E_j$$

Fig 2.2 Three-port network representation of an interdigital transducer. [2]

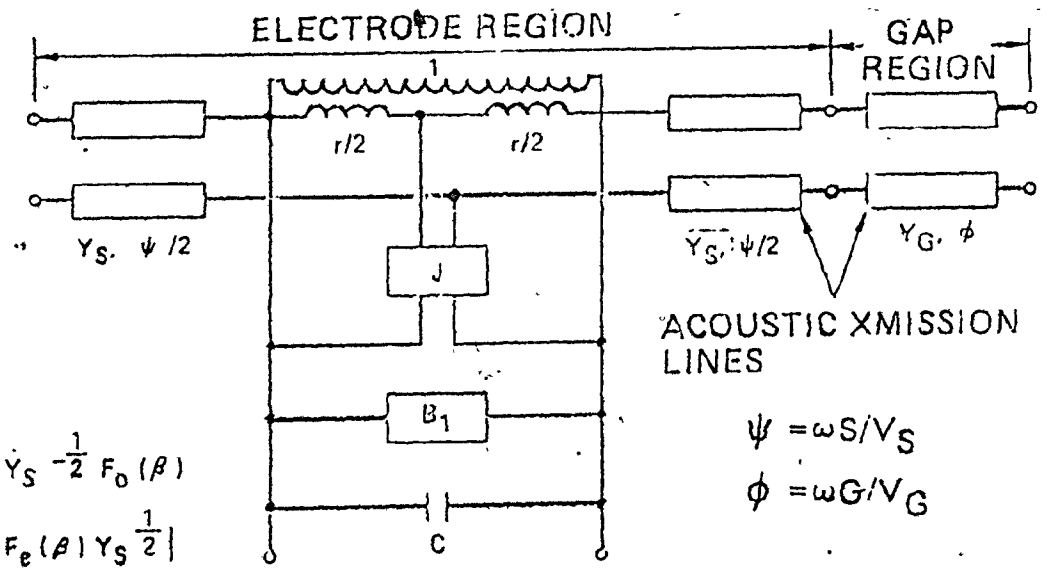

$$r = j\beta Y_S^{-\frac{1}{2}} F_0(\beta)$$

$$J = |\beta F_e(\beta) Y_S^{\frac{1}{2}}|$$

$$B_1 = \frac{1}{2} H\left(|\beta F(\beta)|^2\right)$$

Fig 2.3 Generalized circuit model for one section (one electrode and adjacent gap) in an interdigital transducer. [2]

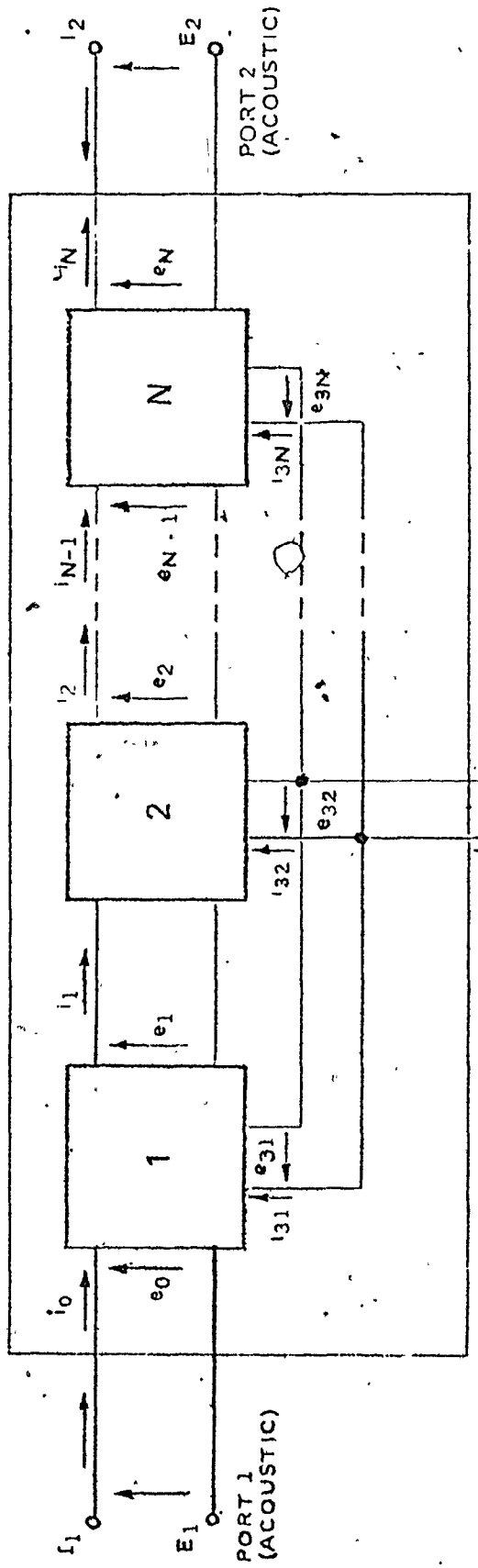

Fig 2.4 Network for a transducer composed of N sections (electrodes), acoustically in cascade and electrically in parallel. [2]

2.2.1 Calculation of y_{ij}

To compute the values of y_{ij} the elements of the generalized circuit model for each section (electrode and adjacent gap) shown in Figure 2.3 must first be evaluated. The circuit elements are found by developing expressions for the electric fields under any one electrode in any local environment. The electric fields are found by solving a set of electrostatic boundary value problems, and by making the assumptions that:

(i) the fields in the region of an electrode depend only on the dimensions and polarities of that electrode and its nearest and next-nearest neighbours.

(ii) the electrode widths and spacings within the local environment are either all identical or vary so slowly from electrode to electrode that all electrodes within the local environment may be considered to have the same metallization ratio, η

(iii) the electrodes are all infinitesimally thin perfect conductors.

With these assumptions it can be proved, as shown in Appendix I of [7], that the normalized electric field for the ith electrode is:

$$\frac{E_z(x_i,\eta_i)\ |z=0}{(\Delta V/L_i)} = -\frac{AL_i}{2}\sum_{m=0}^{5}(\eta_i - 0.5)^m \cdot$$

$$\sum_{n=1}^{5}\alpha_{nm}(p_i)\ \frac{T_n(2x_i/\eta_i L_i)}{[(\eta_i L_i/2)^2 - x_i^2]^{\frac{1}{2}}} \qquad (2.2)$$

where,

T_n = Chebyshev polynomial of order n

η_i = metallization ratio of ith electrode

A = dielectric constant ratio

$$= 2\pi[\varepsilon_{xx}/\varepsilon_{zz} - \varepsilon_{xz}^2/\varepsilon_{zz}^2]^{\frac{1}{2}} \qquad (2.3)$$

= 15.71 for YZ -lithium niobate crystal

where, ε_{xx}, ε_{zz}, ε_{xz} = dielectric constants of crystal

$\alpha_{nm}(p_i)$ is a set of coefficients for a corresponding local polarity sequence, p_i, around electrode i. These coefficients are listed in Appendix II of [7].

The element C_i of Figure 2.3, is the capacitance associated with the charge and voltage on the ith electrode. C_i is found by integrating the charge density distribution (the double summation in equation (2.2)) from $x_i = -\eta_i L_i/2$ to $x_i = \eta_i L_i/2$, giving,

$$C_i = \frac{|Q_i|}{(\Delta V)} = \frac{\pi A}{2}\varepsilon_{zz}\left[\sum_{m=0}^{5}\alpha_{om}(p_i)(\eta_i - \tfrac{1}{2})^m\right] \qquad (2.4)$$

The acoustic transit angle in the electrode region,

$$\psi = \omega S/v_s \tag{2.5}$$

where S = width of electrode

and v_s = acoustic velocity under the electrode

The acoustic transit angle in the gap region,

$$\psi = \omega G/v_G \tag{2.6}$$

where G = width of gap

and v_G = acoustic velocity in the gap

The transformer ratio, r_i, is given by,

$$r_i = j\beta Y_s - \tfrac{1}{2}F_{io}(\beta) \tag{2.7}$$

where,

$$\beta = \text{wavenumber} = 2\pi f/v \tag{2.8}$$

Y_s = characteristic mechanical admittance in the electrode region.

$F_{io}(\beta)$ = the imaginary part of the spectral excitation function.

i.e. $F_i(\beta) = F_{ie}(\beta) + jF_{io}(\beta)$

$$F_i(\beta) = \left[\frac{4}{\pi}\frac{\beta_0}{\beta} f_i k_0^2 C_i \,|_{\eta_i=\frac{1}{2}}\right]^{\frac{1}{2}} \cdot \mathfrak{F}\left\{\frac{2\pi}{A} \cdot \frac{E_z(x_i,\eta_i)|_{z=0}}{(\Delta V/L_i)}\right\}$$

$$= \left[\frac{4}{\pi}\frac{\beta_0}{\beta} f_i k_0^2 C_i \,|_{\eta_i=\frac{1}{2}}\right]^{\frac{1}{2}} \cdot \pi^2 L_i \cdot \sum_{m=0}^{5} (\eta_i - \tfrac{1}{2})^m$$

$$\cdot \sum_{n=0}^{5} \alpha_{nm}(p_i)(-j)^n J_n\left(\frac{\beta\eta_i L_i}{2}\right) \tag{2.9}$$

where,

β_0 = reference wavenumber

$$= \pi/L_i \tag{2.10}$$

J_n = cylindrical Bessel function of order n.

f_i = half-wavelength frequency of the ith electrode

$$= \frac{v}{2L_i} \tag{2.11}$$

k_0^2 = intrinsic substrate coupling constant

$$= 2\Delta v/v \tag{2.12}$$

where $\Delta v/v$ is the fraction velocity change calculated by Campbell and Jones [29] and $\mathcal{F}$ denotes the Fourier transform.

In the generalized equivalent circuit model J_i acts as a quarter wave transmission line at all frequencies, and has the form:

$$J_i = |F_{ie}(\beta)Y_s^{\frac{1}{2}}| \tag{2.13}$$

where $F_{ie}(\beta)$ is the real part of the spectral excitation function $F_i(\beta)$.

The shunt element jB_{il} is given by:

$$B_{il} = \tfrac{1}{2}\mathcal{H}(|\beta F_i(\beta)|^2) \tag{2.14}$$

where $\mathcal{H}$ denotes the Hilbert transform.

Now that all the circuit elements of Figure 2.3 are stated, the admittance coefficients y_{ij} can easily be found by circuit analysis, and are given as:

$$y_{11} = y_{22} = -jY_s \cot\Psi \tag{2.15}$$

$$y_{12} = jY_s \csc\Psi \tag{2.16}$$

$$y_{13} = -j \frac{Y_s^{\frac{1}{2}}\beta}{2} \exp[-j(\Psi/2)] \left[(1-j\cot\Psi)F_i(\beta) + j\csc\Psi F_i^*(\beta)\right] \tag{2.17}$$

$$y_{23} = -j \frac{Y_s^{\frac{1}{2}}}{2} \exp[-j(\Psi/2)] \left[j\csc\Psi F_i^*(\beta)\right] \tag{2.18}$$

$$y_{33} = j\omega C_i + jB_{il} + j\frac{\beta^2}{2}\left[\cot\frac{\Psi}{2} F_{io}^2(\beta) + \tan\frac{\Psi}{2} F_{ie}^2(\beta)\right] \tag{2.19}$$

$$y_{ij} = y_{ji} \tag{2.20}$$

2.2.2 Calculation of Y_{ij}

The three port matrix for the entire transducer is found by connecting the N sections in cascade acoustically and in parallel electrically, as shown in Figure 2.4.

Define $Y_{ij}(N)$ as the admittance coefficients of a transducer consisting of N sections (electrodes), and $Y_{ij}(n)$ as the admittance coefficients of the Nth section in the transducer.

For N = 1

$$Y_{ij}(1) = y_{ij}(1) \tag{2.21}$$

For N > 1, the recursion relations |10| give,

$$Y_{11}(N) = y_{11}(n) - \frac{[y_{12}(n)]^2}{D} \tag{2.22}$$

$$Y_{12}(N) = \frac{-y_{12}(n)Y_{12}(N-1)}{D} \tag{2.23}$$

$$Y_{22}(N) = Y_{22}(N-1) - \frac{Y_{12}(N-1)^2}{D} \tag{2.24}$$

$$Y_{13}(N) = y_{13}(n) - \frac{y_{12}(n)y'}{D} \tag{2.25}$$

$$Y_{23}(N) = Y_{23}(N-1) - \frac{Y_{12}(N-1)y'}{D} \tag{2.26}$$

$$Y_{33}(N) = y_{33}(n) + Y_{33}(N-1) - \frac{(y')^2}{D} \tag{2.27}$$

$$Y_{ij}(N) = Y_{ji}(N) \tag{2.28}$$

where

$$D = y_{22}(n) + Y_{11}(N-1) \tag{2.29}$$

and

$$y' = y_{23}(n) + Y_{13}(N-1) \tag{2.30}$$

For the calculation of the transfer function, $T_{13}(f)$, the transducer radiation admittance term, $Y_{rad}(f)$, must be found. In terms of Y_{ij},

$$Y_{rad}(f) = (Y_{33}-j\omega C_T)-\tfrac{1}{2}(Y_{13}^2+Y_{23}^2)+\frac{Y_{12}Y_{13}Y_{23}}{1+Y_{11}} \tag{2.31}$$

where

$$C_T = \text{transducer total static capacitance} = \sum_{i=1}^{N} C_i \tag{2.32}$$

Now through the use of the formulas given above and a digital computer, the frequency response of a transducer with any metallization ratio and polarity sequences can be accurately calculated at the fundamental and higher harmonic frequencies.

CHAPTER III

HIGHER HARMONIC MODE GENERATION IN SAW TRANSDUCERS

3.1 General

This chapter will investigate the means of higher harmonic mode generation using the three most commonly used transducer geometries shown in Figure 3.1. The relative amplitudes of several higher harmonics will be illustrated as a function of metallization ratio for each of the three different transducer geometries. Then the problems associated with operating a SAW transducer at higher harmonics will be discussed.

3.2 Harmonic Amplitude Levels in the 2-Finger Transducer

Engan [4] computed the various spatial harmonics in a 2-finger transducer by finding the Fourier components of the electric field distribution. The electric field distribution was found using the assumptions of small piezoelectric coupling, infinitely long transducer, and negligible thickness of metal fingers. For the transducer structure shown in Figure 3.2(a) and the boundary conditions of one half-period shown in Figure 3.2(b) when a potential V_0 is

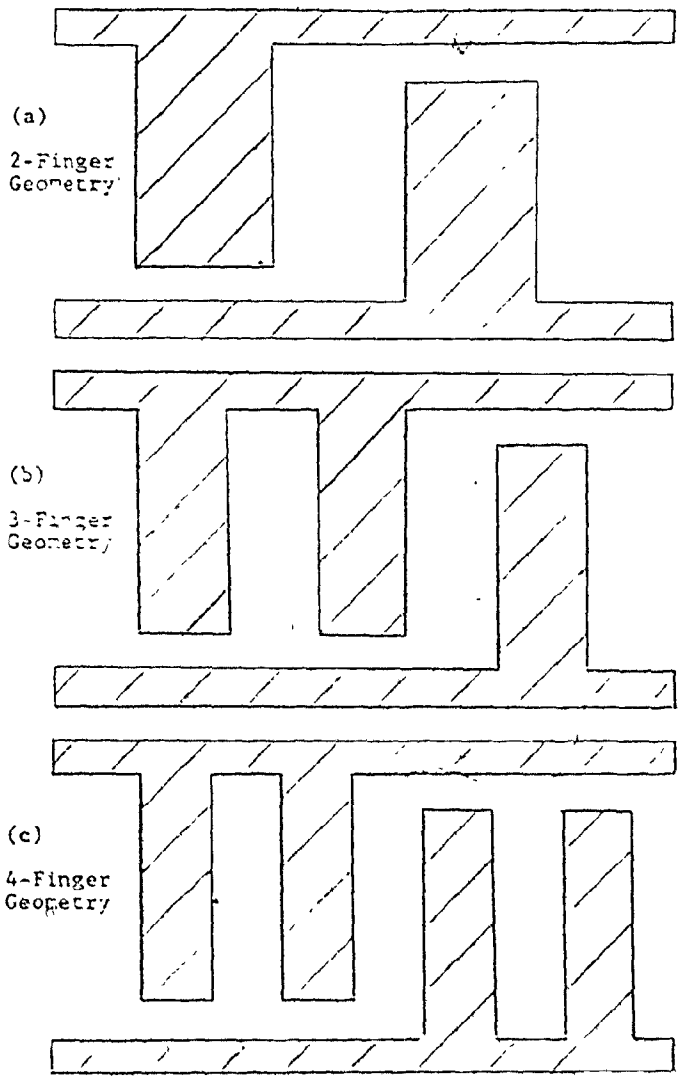

Fig. 3.1 The three most commonly used finger geometries for SAW transducers.

(a) 2-Finger geometry
(b) 3-Finger geometry
(c) 4-Finger geometry

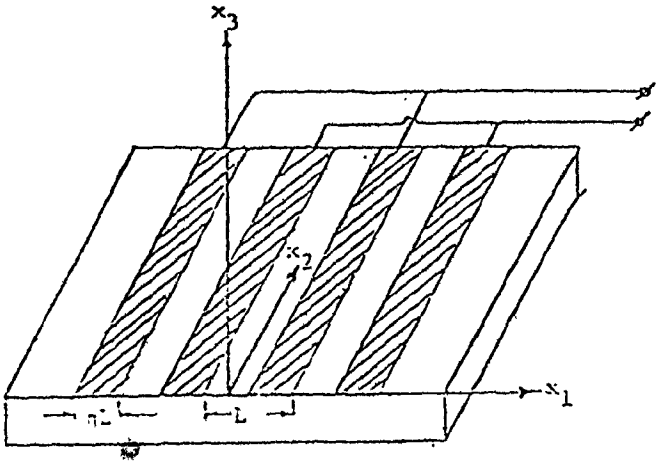

(a)

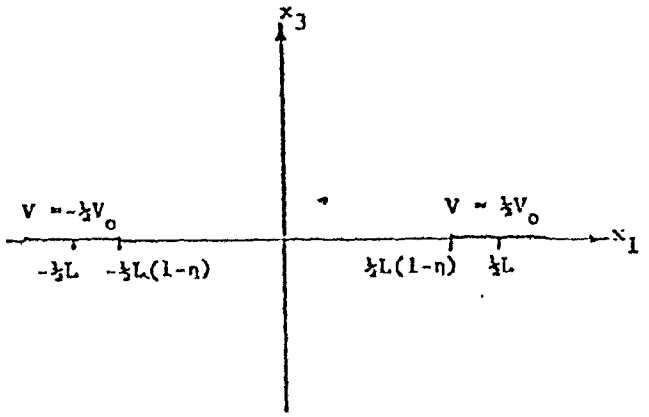

(b)

Fig. 3.2 (a) Two-finger transducer surface arrangement.
[4] (b) Boundary conditions.

applied to the transducer terminals, the electrical potential must satisfy Poisson's equation:

$$\varepsilon_{11} \frac{\partial^2 V}{\partial x_1^2} + 2\varepsilon_{13} \frac{\partial^2 V}{\partial x_1 \partial x_3} + \varepsilon_{33} \frac{\partial^2 V}{\partial x_3^2} = 0 \tag{3.1}$$

subject to the boundary conditions

$$V = \pm \tfrac{1}{2} V_o \quad \text{for } x_3 = 0 \tag{3.2}$$

and $\tfrac{1}{2}L(1-\eta) \leq \pm x_1 < \tfrac{1}{2}L$

where (x_1, x_2, x_3) refers to the crystal coordinate system. Since V and D_3 are both continuous

$$D_3 = -\varepsilon_{13} \frac{\partial V}{\partial x_1} - \varepsilon_{33} \frac{\partial V}{\partial x_3} \tag{3.3}$$

for $x_3 = 0$
and $|x_1| < \tfrac{1}{2}L(1-\eta)$

The potential on the surface ($x_3=0$) must satisfy the symmetry relation

$$V(x_1+L) = -V(x_1)$$

The potential below the surface ($x_3<0$) can be written as the sum

$$V = -\sum_{n=0}^{\infty} \frac{L}{\pi(2n+1)} A_{2n+1} \sin\left\{(2n+1)\frac{\pi}{L}\right.$$

$$\left.\cdot\,(x_1 - \frac{\varepsilon_{13}}{\varepsilon_{33}} x_3 + \delta_n)\right\} \exp\left\{(2n+1)\frac{\pi}{L}\varepsilon_r x_3\right\} \qquad (3.4)$$

where

$$\varepsilon_r = (\varepsilon_{11}/\varepsilon_{33} - \varepsilon_{13}^2/\varepsilon_{33}^2)^{\frac{1}{2}}$$

A_{2n+1} is the amplitude of the $(2n+1)$th harmonic and δ_n is a phase constant.

Thus the tangential component of the electric field

$$E_1 = \sum_{n=0}^{\infty} A_{2n+1} \cos\left\{(2n+1)\frac{\pi}{L}\right.$$

$$\left.\cdot\,(x_1 - \frac{\varepsilon_{13}}{\varepsilon_{33}} x_3 + \delta_n)\right\} \exp\left\{(2n+1)\frac{\pi}{L}\varepsilon_r x_3\right\} \qquad (3.5)$$

and the normal component of the electric displacement

$$D_3 = \sum_{n=0}^{\infty} \varepsilon_{33}\,\varepsilon_r A_{2n+1} \sin\left\{(2n+1)\frac{\pi}{L}\right.$$

$$\left.\cdot\,(x_1 - \frac{\varepsilon_{13}}{\varepsilon_{33}} x_3 + \delta_n)\right\} \exp\left\{(2n+1)\frac{\pi}{L}\varepsilon_r x_3\right\} \qquad (3.6)$$

Since the electric field must be zero at the electrodes from the boundary condition given in equation (3.2)

$$\sum_{n=0}^{\infty} A_{2n+1}\cos(2n+1)\frac{\pi}{L}(x_1 + \delta_n) = 0 \qquad (3.7)$$

when $\frac{1}{2}L\ (1-\eta) \leq \pm x_1 < \frac{1}{2}L$

Since D_3 is continuous across the surface ($x_3=0$) between the electrode gap ($|x_1| < \frac{1}{2}L(1-\eta)$)

$$\sum_{n=0}^{\infty} A_{2n+1}\sin(2n+1)\frac{\pi}{L}(x_1 + \delta_n) = 0 \qquad (3.8)$$

Equations (3.7) and (3.8) are both satisfied when

$\delta_n = 0$

and $A_{2n+1} = BP_n(\cos\pi(1-\eta)$ (3.9)

where B is a constant determined by V_o

and P_n is the Legendre function of the first kind.

Equation (3.9) shows that the amplitude of any harmonic depends on the metallization ratio, η, of the fingers in the transducer. Thus the choice of metallization ratio is very important when operating at a higher harmonic mode. For example the amplitude of the 3rd harmonic (n=1) for a metallization ratio of 0.5 ($\eta = 0.5$) is found from equation (3.9) to be

$$A_{2(1)+1} = BP_1(\cos\pi(1-0.5))$$

$$\therefore A_3 = BP_1(\cos\pi(0.5) = BP_1(0)$$

but $P_1(x) = x$

$$A_3 = B.0 = 0$$

Therefore the amplitude of the 3rd harmonic is zero for a 2-finger transducer of metallization ratio 0.5.

A plot of A_{2n+1} versus metallization ratio is shown in Figure 3.3 for the five lowest harmonics.

3.3 Harmonic Amplitude Levels in 3- and 4-Finger Transducer

Using the same assumptions and field theories outlined in the preceding section Kerbel [11] computed the amplitude of 15 lowest spatial harmonics of the 3-finger transducer as a function of metallization ratio, as shown in Figure 3.4. Hunsinger et. al. [12] also recently computed a similar plot using a generalized model for finite periodic transducers. Note that even harmonics are possible for the 3-finger transducer unlike the cases for the 2- and 4-finger transducers.

The amplitude of the spatial harmonics as a function of metallization ratio for the 4-finger transducer, as shown in Figure 3.5, was first derived by Hartmann and Secrest [13] by solving the field equations using an iterative technique on a digital computer and Fast Fourier Transform routines for finding the corresponding A_{2n+1}.

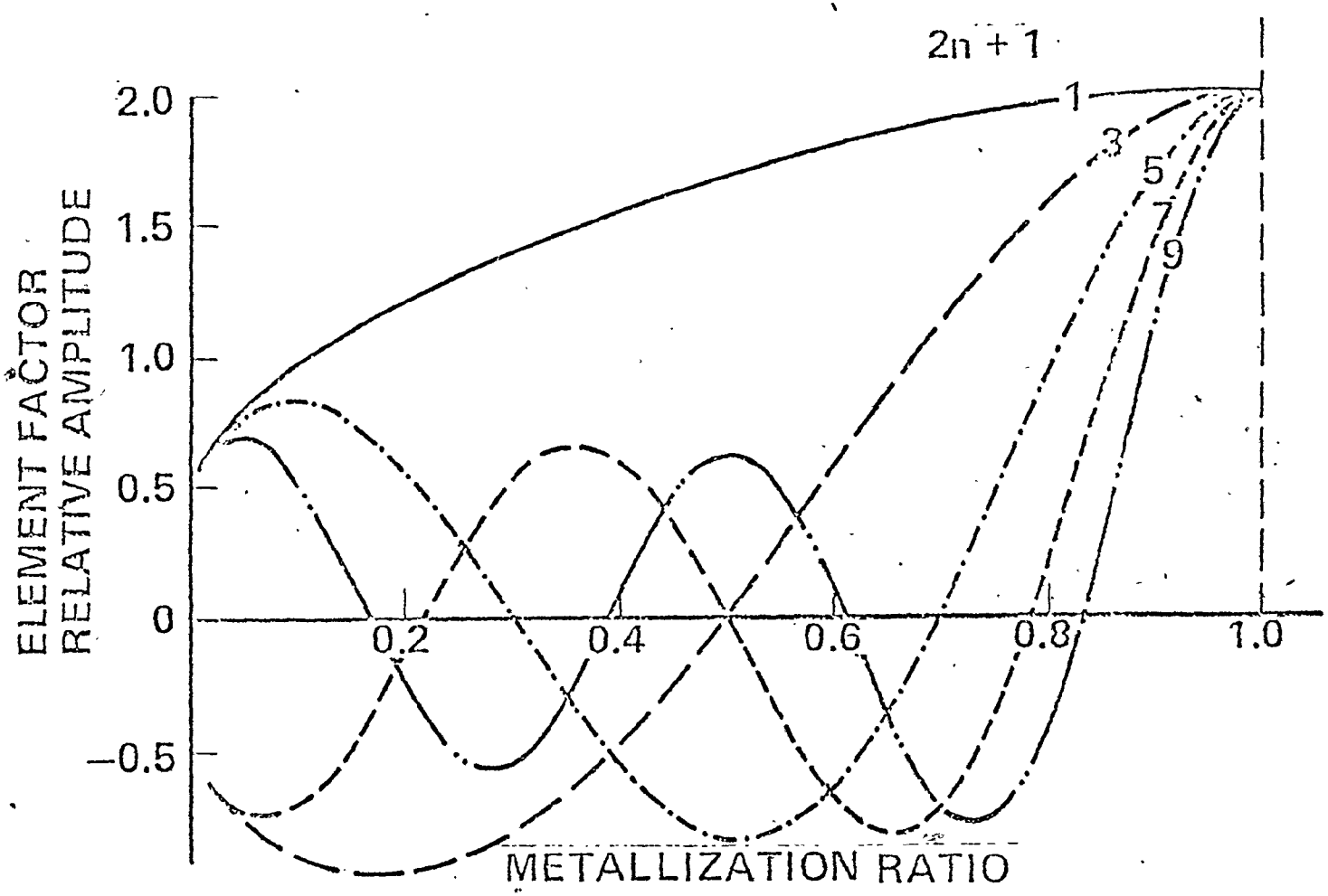

Fig. 3.3 Amplitude of the five lowest spatial harmonics as a funetion of n for the 2-finger geometry transducer.
[2]

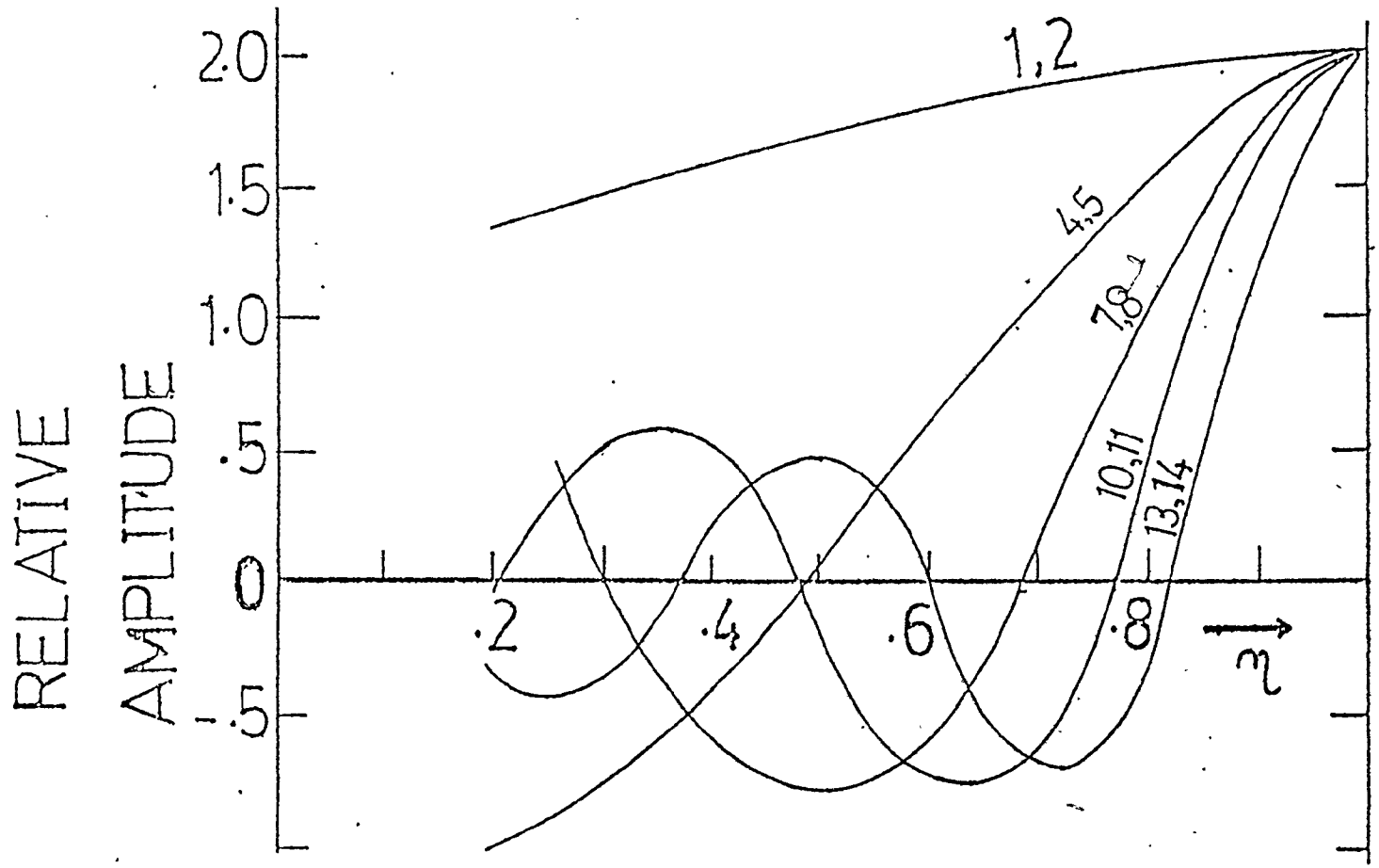

Fig. 3.4 Amplitude of 15 lowest spatial harmonics of the 3-finger geometry transducer.

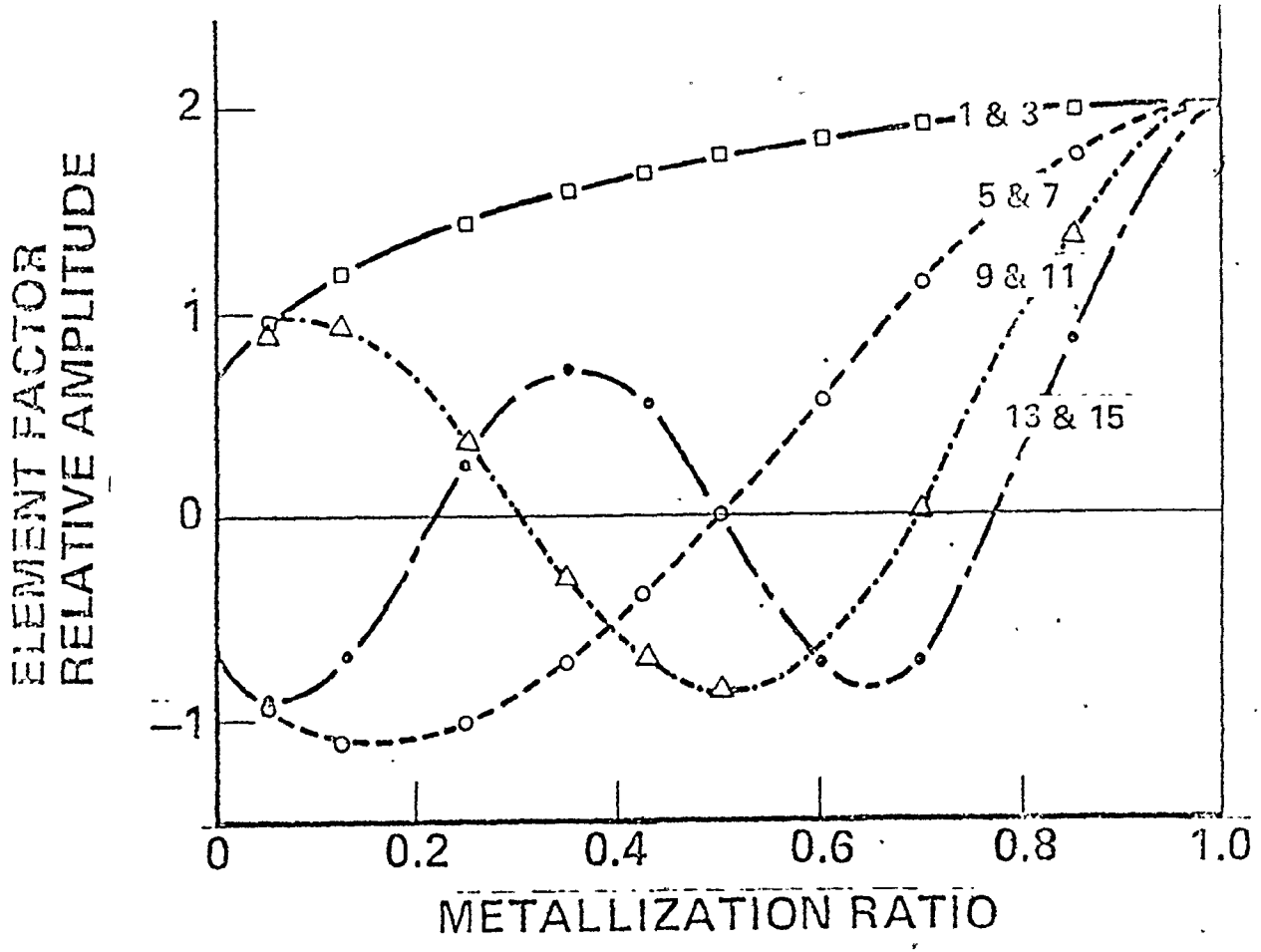

Fig. 3.5 Amplitude of 15 lowest spatial harmonics of the 4-finger geometry transducer.

Smith and Pedler [7] used their generalized circuit model to theoretically determine the insertion loss (output signal amplitude divided by input signal amplitude) for 4-finger transducers with metallization ratios of 0.58 and 0.9.

The insertion loss [7] for an untuned transducer is given as

$$IL = -20 \log_{10} \frac{2G_L G_a(f)}{(G_L+G_a(f))^2+(2\pi f C_T)^2} \qquad (3.10)$$

where G_L = source conductance

$G_a(f)$= radiation conductance found from eq. (2.31)

C_T = total capacitance found from eq. (2.32)

Figures 3.6 and 3.7 show the theoretical and experimental results obtained for uniform transducers with metallization ratios of 0.58 and 0.9 respectively. Both transducers' aperture, W, was chosen so that the insertion loss at the 9th harmonic was minimized at the expense of higher insertion loss at the other harmonics.

As predicted by the plots in Figure 3.5 the 5th and 7th harmonics have the lowest amplitudes for a metallization ratio of 0.58; this is verified in Figure 3.6.

Figure 3.5 also predicts that the amplitude of all the harmonics will be approximately equal at a metallization

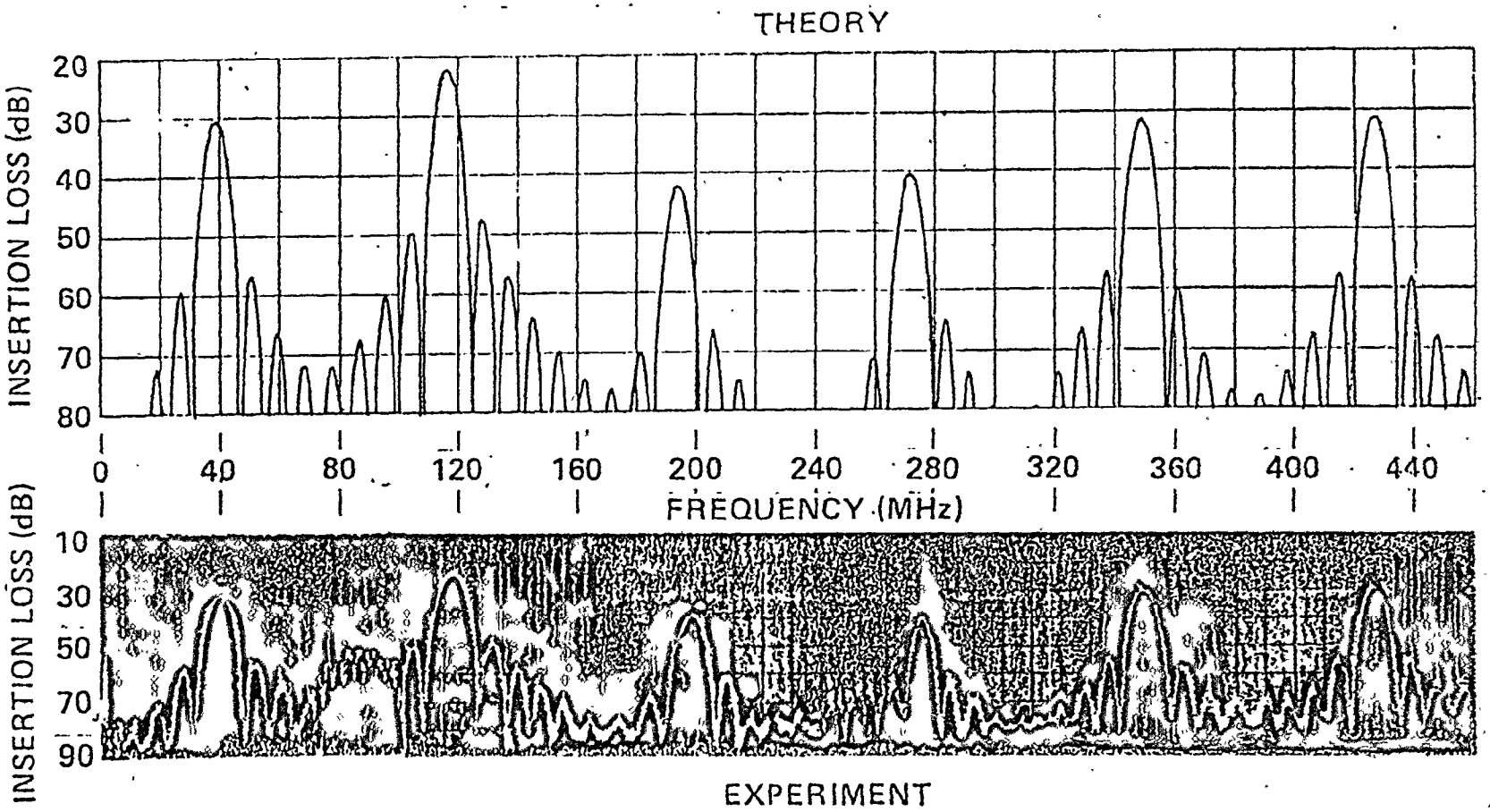

Fig.3.6 Theoretical and experimental insertion loss of spatial harmonics in a 4-finger transducer of metallization ratio 0.58. [2]

ratio of 0.9; this is verified in Figure 3.7.

Note also that the corresponding harmonic levels are higher for a metallization ratio of 0.9. This also was predicted by the plots in Figure 3.5.

3.4 Problems Associated with Higher Harmonic Mode Operation

There are two major problems arising out of higher harmonic mode operation. The first is changes in the coupling factor, k^2, from the intrinsic substrate coupling factor, k_0^2. The effective coupling factor for the Mth harmonic is defined by

$$k_{eff}^2 = \frac{\pi Q_r^{-1}}{2N} \tag{3.11}$$

where

N = total number of electrodes

Q_r = radiation Q

$$= \frac{2\pi f_M C_T}{G_a(f_M)} \tag{3.12}$$

f_M is the frequency of the Mth harmonic mode.
C_T and $G_a(f_M)$ can be accurately calculated from the generalized circuit model as outlined in Chapter II. Thus k_{eff}^2 for any higher harmonic mode, metallization ratio and given transducer geometry may be calculated. Figures 3.8 and 3.9 [7] show how k_{eff}^2 for the 11 lowest harmonics vary with

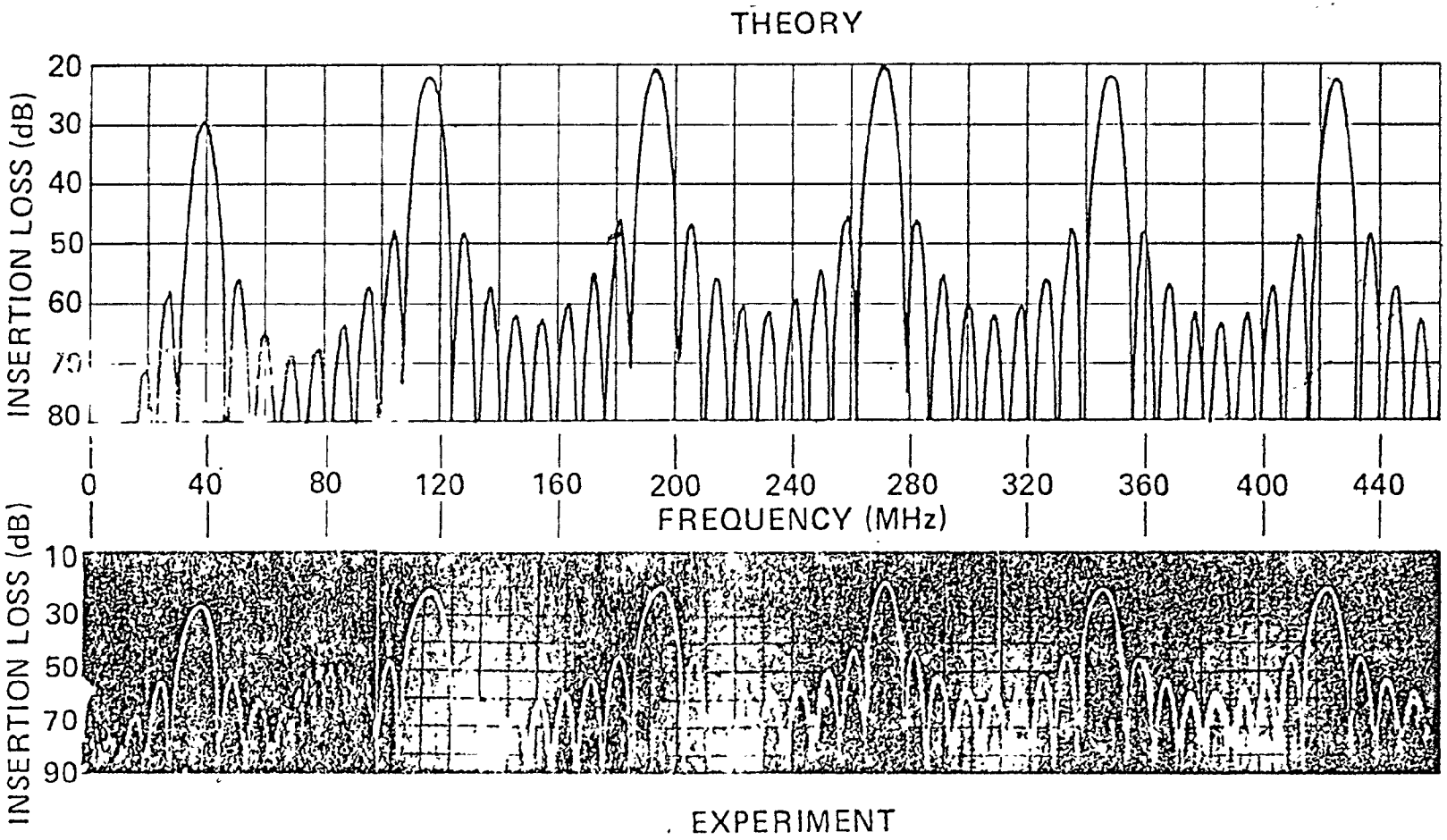

Fig.3.7 Theoretical and experimental insertion loss of spatial harmonics [2] in a 4-finger transducer of metallization ratio 0.9.

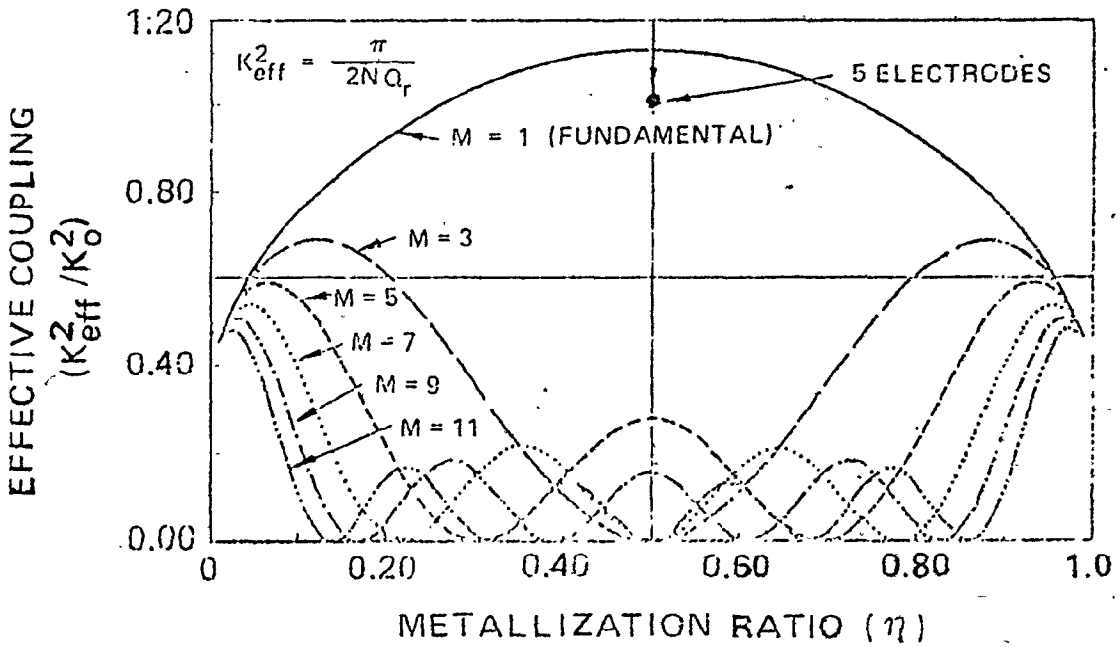

Fig. 3.8 k^2_{eff} versus metallization ratio for a 2-finger periodic transducer. [2]

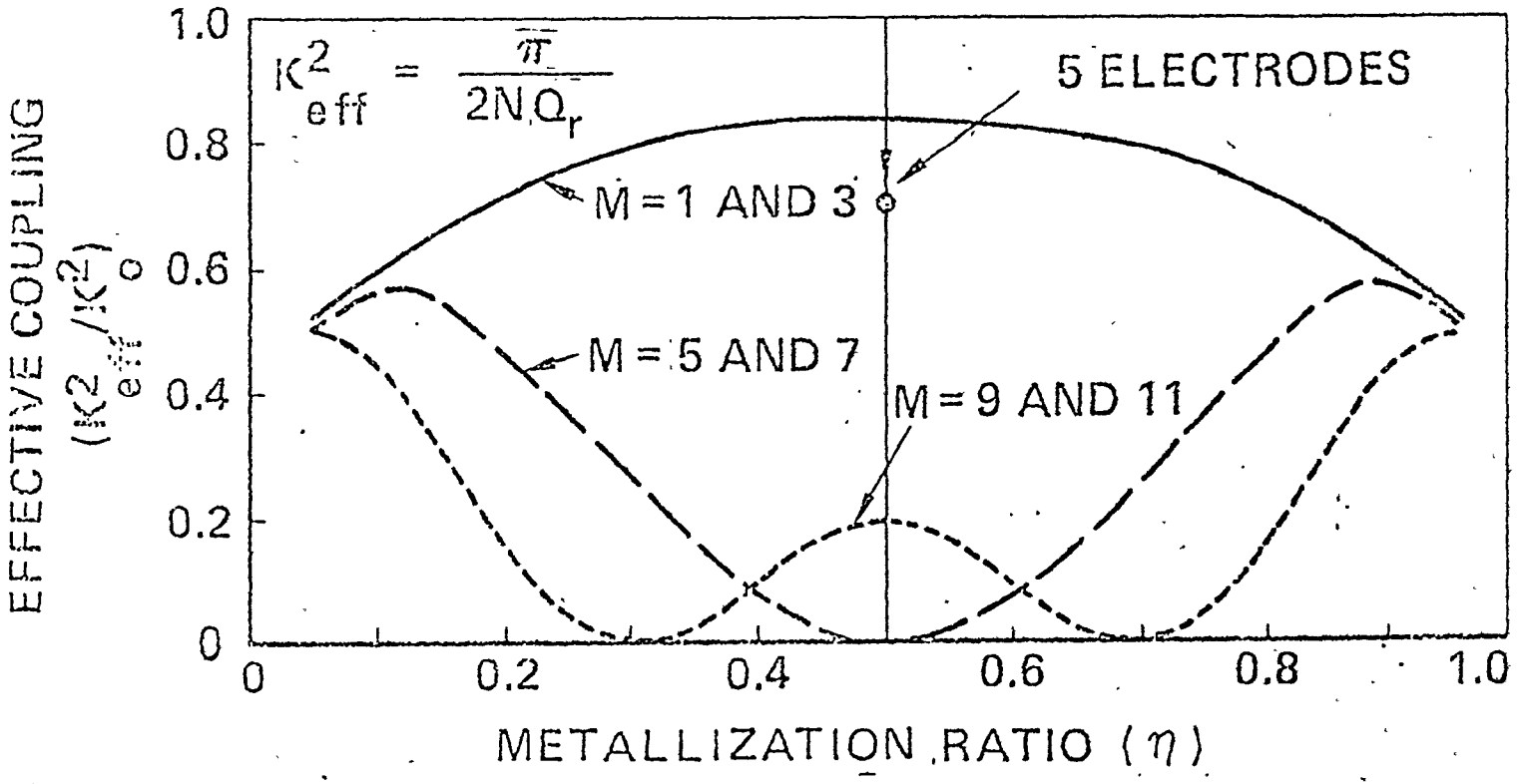

Fig. 3.9 k^2_{eff} versus metallization ratio for a 4-finger periodic transducer. [2]

metallization ratio for the 2- and 4-finger transducer geometry respectively. The curves coincide well with experimental points given in [14]. The large dot on Figure 3.8 and 3.9 shows k^2_{eff} for the fundamental mode at a metallization ratio of 0.5 when a short transducer of only 5 electrodes is used.

The second and more difficult problem arising from the use of transducers operating at a higher harmonic mode is that of interference from other harmonic modes. Inspection of the plots given in Figures 3.3, 3.4 and 3.5 will shown that at any given metallization ratio more than one harmonic mode will be generated. This fact is experimentally verified by Figures 3.6 and 3.7.

The following chapters contain detailed discussions on the solutions for isolating the desired harmonic mode from the remaining modes.

CHAPTER IV

SOLUTIONS TO HIGHER HARMONIC MODE SELECTION

4.1 General

In the last chapter it was shown how higher harmonic modes may be generated in SAW transducers by proper selection of metallization ratio. It was also seen that more than one harmonic mode will be generated for any given metallization ratio. Before 1974 narrow band filters external to the SAW device were used to select the desired harmonic mode from the remaining harmonic modes. The external filtering devices however added the problems of frequency alignment, phase sensitivity and increased size and weight. In 1974 Kerbel [11] and Engan [15] simultaneously disclosed a technique for harmonic mode selection without the use of external filtering devices. They did so by utilizing the harmonic responses of different finger geometries. For example, the input transducer was of a 4-finger geometry and the output transducer a 3-finger geometry. This method of internal filtering works well, but at high frequencies the lithographic problems arise again since this method must use the 3- or 4-finger geometries or both.

The ultimate goal for higher harmonic frequency operation with internal mode selection would be for the utilization of the 2-finger geometry in both input and output transducers, since this structure gives the maximum linewidth for any given fundamental frequency. This was the major purpose for the studies reported in this thesis.

One of the solutions the author came up with was the use of 2-finger input and output transducers, separated by a multistrip coupler [16] - [19], which was specially designed to have its pass band coincide with the pass band of the desired harmonic mode. A detailed account of this method is given in Appendix I.

A more efficient method was later found by the author. This method also employs the 2-finger geometry for both input and output transducers, but does not require the use of a multistrip coupler. But the fingers of the 2-finger transducer are now stepped rather than simply straight.

The theories of Kerbel's and Engan's 3- and 4-finger solution and the author's stepped-finger solution are outlined in detail in the following sections of this chapter.

4.2 Kerbel's and Engan's Solution

This solution depends on the different harmonic responses of different finger geometries. The technique works because it staggers the harmonic responses of the two transducers so that they only overlap in one frequency band. For example

a 4-finger geometry may be used for the input transducer and a 3-finger geometry for the output transducer as shown in Figure 4.1. If both transducers have a metallization ratio of 0.5, reference to Figures 3.4 and 3.5 will show that the 4-finger input transducer will generate its 1st, 3rd, 9th and 11th harmonics, while the 3-finger output transducer will detect its 1st, 2nd, 7th, 8th, 13th and 14th harmonics. If the 11th harmonic frequency of the 4-finger transducer is chosen to equal the 8th harmonic frequency of the 3-finger transducer, then none of the remaining harmonic frequencies of the two transducers will coincide, as shown in Figure 4.2(a). As a result the overall response will be that of the desired frequency band only and all the other harmonic frequencies will be suppressed, as shown in Figure 4.2(b).

Using this method Kerbel [11] was able to build a 1 GHz harmonic SAW oscillator. The suppression obtained for undesired harmonics in this oscillator is summarized in Figure 4.3. Later Temmyo and Yoshikawa [20] successfully built a 2 GHz harmonic SAW oscillator using the same technique.

To measure the resolution improvement obtained from operating a multielectrode transducer at a higher harmonic mode, Kerbel [11] defined the Improvement Ratio (IR). IR is the ratio of the finger width of the multielectrode IDT, operating at the Mth harmonic mode and with a metallization

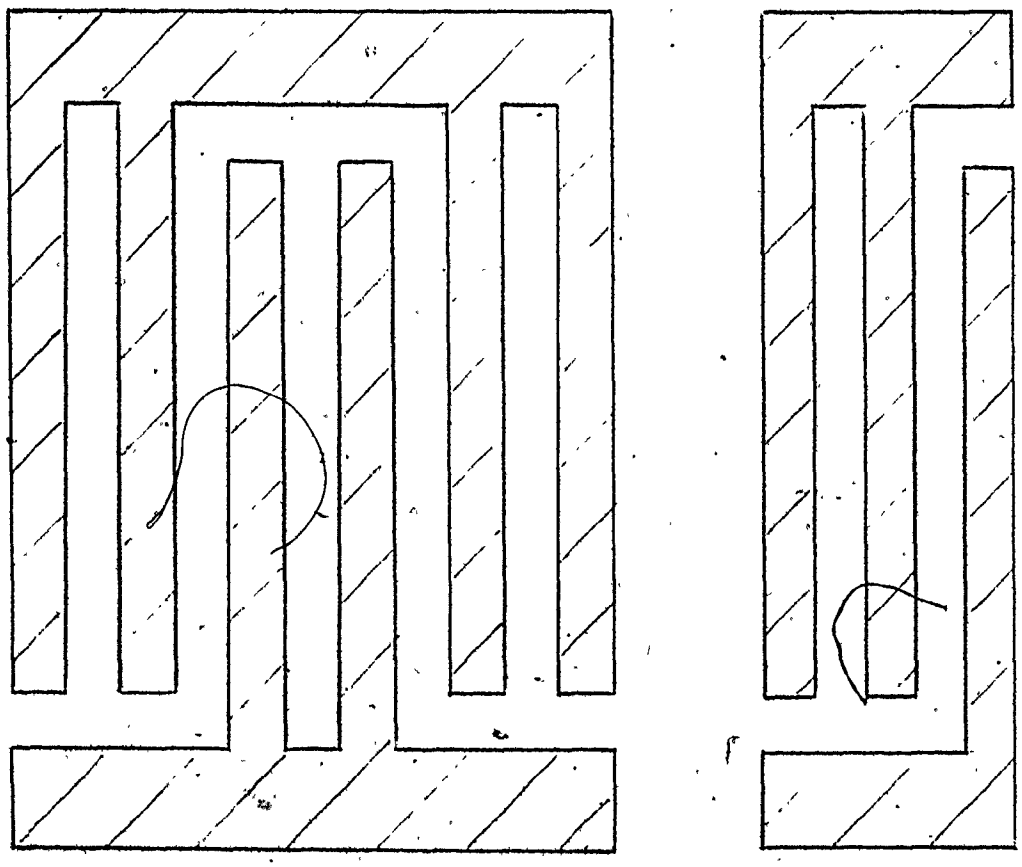

Fig. 4.1 Harmonic filtering using different geometries for input and output transducers.

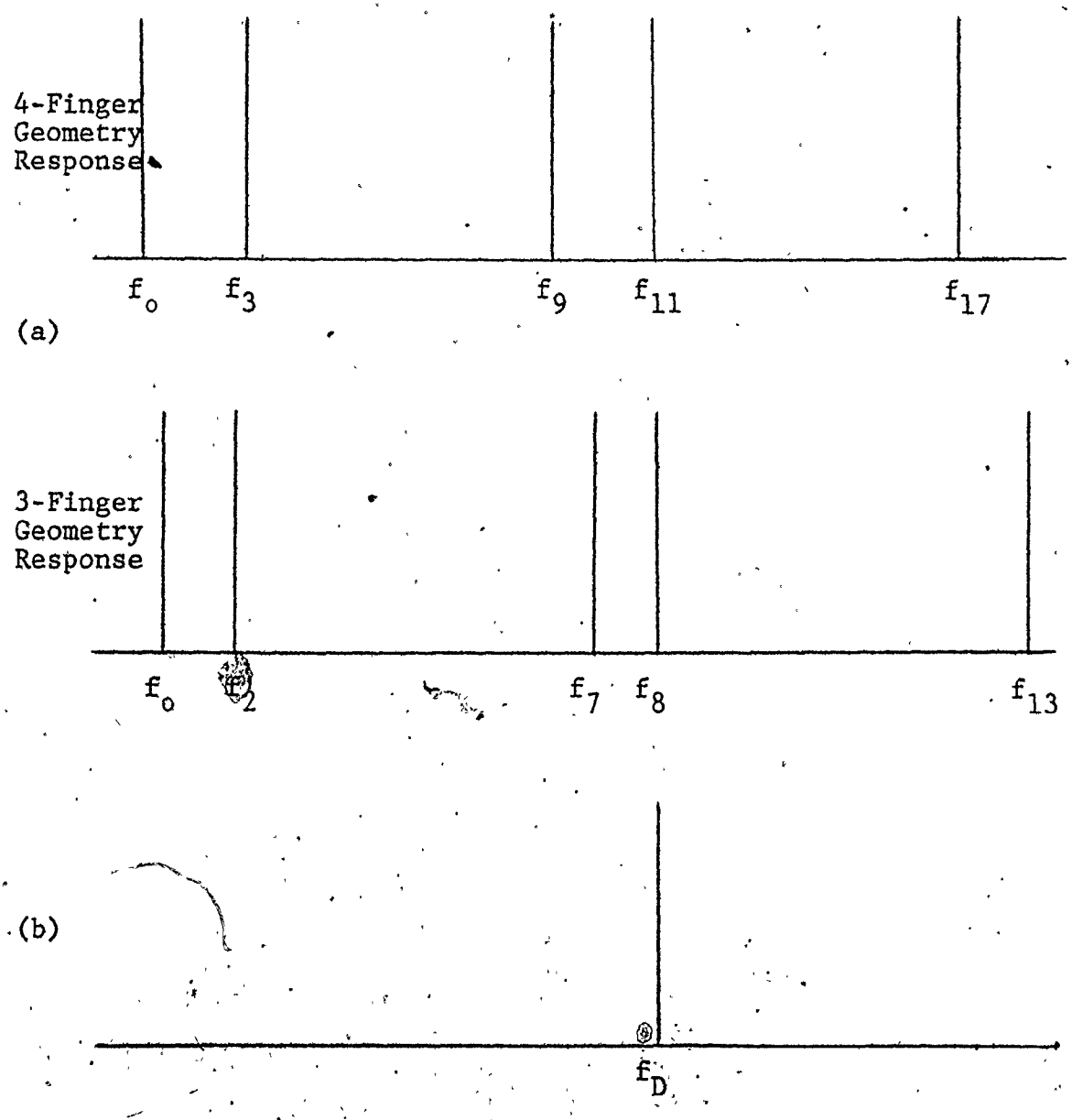

Fig. 4.2 (a) Individual Responses of the two transducers.

(b) Resulting Response from combining the two transducers into one device.

Finger Geometry	Harmonic Mode	Harmonic Frequency MHz	Suppression dB
3, 4	Desired	1027.9	0.0
3	7th	899.4	>40.0
4	9th	841.0	>40.0
4	3rd	280.3	24.0
3	2nd	257.0	31.0
3	Fundamental	128.5	38.0
4	Fundamental	93.4	36.0

Fig. 4.3 Measured Suppression of Harmonics for a 1 GHz SAW Oscillator.

ratio η, to the finger width of a 2-finger transducer of metallization ratio 0.5 and a fundamental frequency equal to the Mth harmonic frequency of the multielectrode transducer, i.e.:

$$IR = \frac{(\lambda_o/NF)\eta}{\frac{1}{4}(\lambda_o/M)}$$

$$= \frac{4M\eta}{NF} \qquad \text{for } \eta \leq 0.5 \tag{4.1}$$

or $$IR = \frac{(\lambda_o/NF)(1-\eta)}{\frac{1}{4}(\lambda_o/M)}$$

$$= \frac{4M(1-\eta)}{NF} \qquad \text{for } \eta \geq 0.5 \tag{4.2}$$

where

NF = number of fingers per wavelength of the multielectrode transducer.

λ_o = fundamental wavelength of the multielectrode transducer.

and η = metallization ratio of the multielectrode transducer.

4.3 The Stepped-Finger Solution

Unlike the classical 2-finger transducer, which has each section along its length at the same phase angle as shown in Figure 4.4(a), the stepped-finger transducer has each of its fingers divided into a particular number of

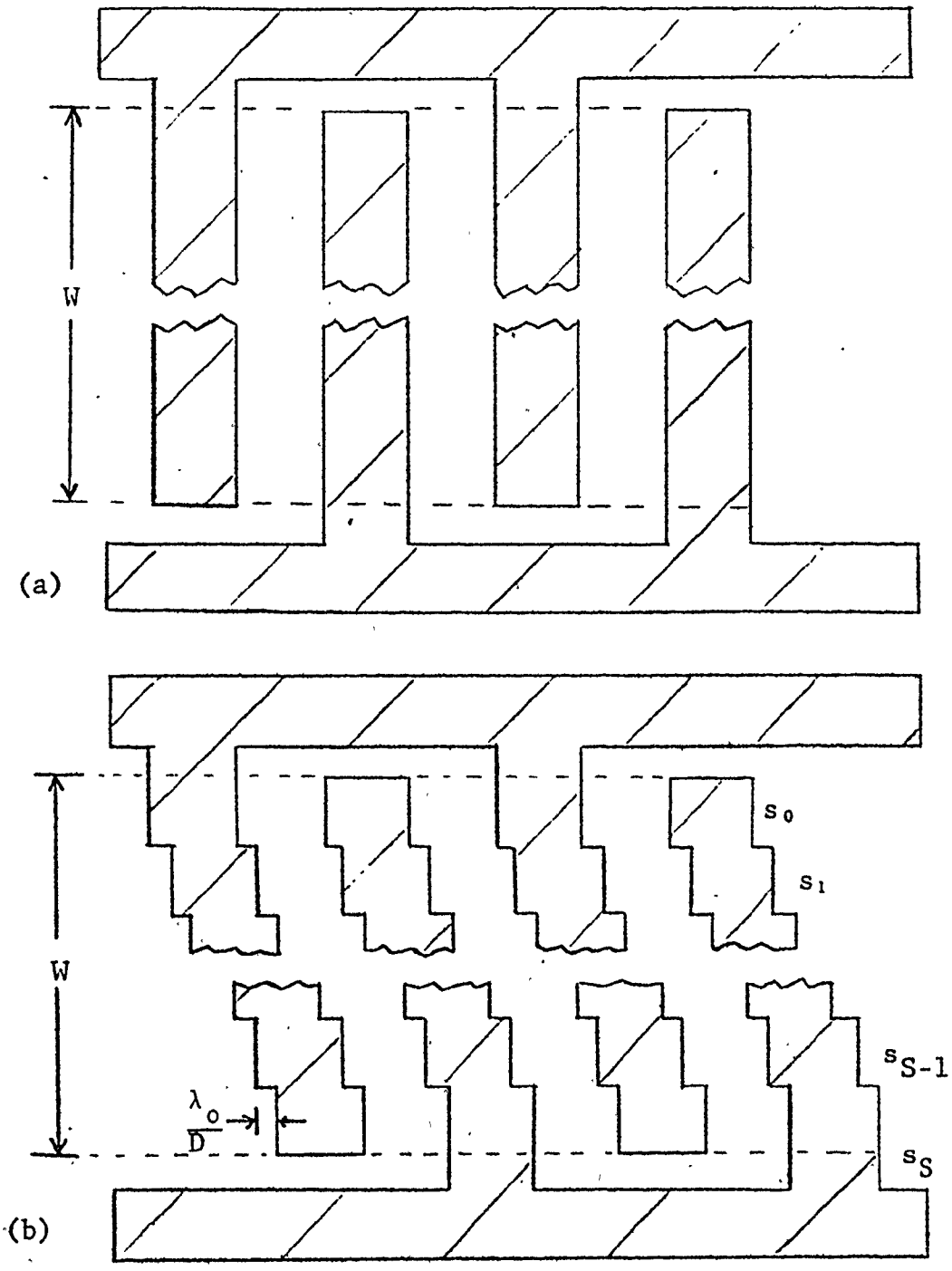

Fig. 4.4 (a) The classical finger structure with each section along its length at the same phase angle.

(b) The stepped-finger structure with each segment along its length displaced from each other by $\frac{\lambda_0}{D}$.

segments (S) and each segment is displaced from each other by a chosen fraction of the fundamental wavelength, $\frac{\lambda_o}{D}$, as shown in Figure 4.4(b). Thus the phase difference between adjacent segments on a finger will be $\frac{2\pi M}{D}$ at any harmonic mode M, where M is assigned the value of 1 for the fundamental harmonic mode, 2 for the second harmonic mode, etc. M_d is the number of the desired harmonic mode.

Let the phase angle of the wave from the 1st stepped segment (s_o) at a summing point P be arbitrarily 0 degrees.

Therefore at summing point P the resultant wave, $R(f_M)$, at any harmonic mode M, will be the phasor sum of the waves generated by each segment:

$$R(f_M) = \sum_{s=0}^{S-1} A(f_M) \; \underline{|s(2\pi M/D)} \qquad (4.3)$$

where S = total number of segments in each finger.

and $A(f_M)$ = amplitude of wave generated by each segment at frequency f_M.

Now if each segment is displaced from each other by $\frac{\lambda_o}{M_d}$ (i.e. $D = M_d$) and each finger is divided equally into M_d segments (i.e. $S = M_d$), then from equation (4.3) the resultant wave at the desired harmonic mode:

$$R(f_{M_d}) = \sum_{s=0}^{M_d-1} A(f_M) \angle s(2\pi M_d/M_d)$$

$$= \sum_{s=0}^{M_d-1} A(f_M) \angle s(2\pi)$$

$$= M_d A(f_M) \quad , \quad (M = M_d) \tag{4.4}$$

And the resultant wave at the undesired harmonic modes:

$$R(f_M) = \sum_{s=0}^{M_d-1} A(f_M) \angle s(2\pi M/M_d)$$

$$= 0 \quad , \quad (M \neq M_d) \tag{4.5}$$

Equations (4.4) and (4.5) indicate that if each finger is divided into M_d number of equal segments and displaced by $\frac{\lambda_o}{M_d}$ from each other, then the waves from each finger will add constructively to the value $M_d A(f_M)$ at the desired harmonic frequency f_{M_d}, but at the other undesired modes the waves will add to zero. Thus, the stepped-finger transducer exhibits internal suppression of all undesired harmonics and passes only the desired mode.

If the uniform receiving transducer of the delay line contains a small number of finger as compared to the stepped-input transducer to be sufficiently broad band, then the

overall response of the delay line will be governed by the stepped-input transducer alone. Tancrell [21] considered a uniform transducer to be analogous to an end-fire antenna array, but with the stepped-finger transducer each finger can be considered as an end-fire antenna. So the transfer function of the stepped-finger transducer, H(f), is the product of the transfer function of the classical uniform transducer, $H_1(f)$, and the transfer function of the stepped-finger, $H_2(f)$.

In the vicinity of a harmonic resonance frequency, f_M, it can be shown [22] that:

$$H_1(f) = A_M \frac{\sin\left[(2\pi N(f-f_M)\right]/f_M}{\left[2\pi N(f-f_M)\right]/f_M}$$

where

N = number of fingers in the transducer

and A_M = the amplitude of the Mth harmonic as determined by the given metallization ratio and other frequency-dependent loss terms.

Considering each stepped-finger as an end-fire antenna array consisting of M_d elements with each element displaced $\frac{\lambda_o}{M_d}$ from its neighbour, the transfer function of this array using the one-sided Z-transform can be expressed as:

$$H_2(z) = a_0+a_1z^{-1}+a_2a^{-2}+.....+a_{M_d-1}z^{-(M_d-1)}$$

$$= \sum_{n=0}^{M_d-1} a_n z^{-n} \tag{4.6}$$

where $z = e^{-j\theta}$

and

$$\theta = 2\,\frac{f-f_{M_d}}{f_{M_d}}$$

since each segment is of the same length, the a_n's are equal. Thus equation (4.6) becomes:

$$H_2(z) = K \sum_{n=0}^{M_d-1} z^{-n} \tag{4.7}$$

where K is a constant. For convenience K is set to 1. Thus:

$$H_2(z) = \sum_{n=0}^{M_d-1} z^{-n}$$

$$= \frac{1-z^{-M_d}}{1-z^{-1}} \tag{4.8}$$

Substituting for z into equation (4.8)

$$H_2(e^{-j\theta}) = \frac{1-e^{jM_d\theta}}{1-e^{j\theta}}$$

$$H_2(\theta) = \frac{1-\cos M_d\theta - j\sin M_d\theta}{1-\cos\theta - j\sin\theta}$$

$$\therefore |H_2(\theta)|^2 = \frac{\sin^2(M_d\theta/2)}{\sin^2(\theta/2)}$$

$$\therefore |H_2(\theta)| = \frac{\sin(M_d\theta/2)}{\sin(\theta/2)} \tag{4.9}$$

Substituting for θ into equation (4.9) we get:

$$|H_2(f)| = \frac{\sin\left[\pi(f-f_{M_d})\right]/f_o}{\sin\left[\pi(f-f_{M_d})\right]/f_{M_d}} \tag{4.10}$$

Thus the magnitude of the overall transfer function for the stepped-finger transducer in the vicinity of any harmonic resonance frequency f_M is given as:

$$|H(f)| = |H_1(f)| \cdot |H_2(f)|$$

$$= A_M \frac{\sin\left[2\pi N(f-f_M)\right]/f_M}{\left[2\pi N(f-f_M)\right]/f_M} \cdot \frac{\sin\left[\pi(f-f_{M_d})\right]/f_o}{\sin\left[\pi(f-f_{M_d})\right]/f_{M_d}} \tag{4.11}$$

Figure 4.5 shows $|H_1(f)|$; $|H_2(f)|$ and $|H(f)|$.

Note that the second term in equation (4.11) will have a value of M_d at the desired harmonic resonance ($f=f_{M_d}$), and a value of zero at all other harmonic resonances ($f\neq f_{M_d}$). Note also for $M_d=1$ (which is necessary to make the stepped-finger transducer the same as the classical uniform transducer) the second term in equation (4.11) becomes unity for all values of f.

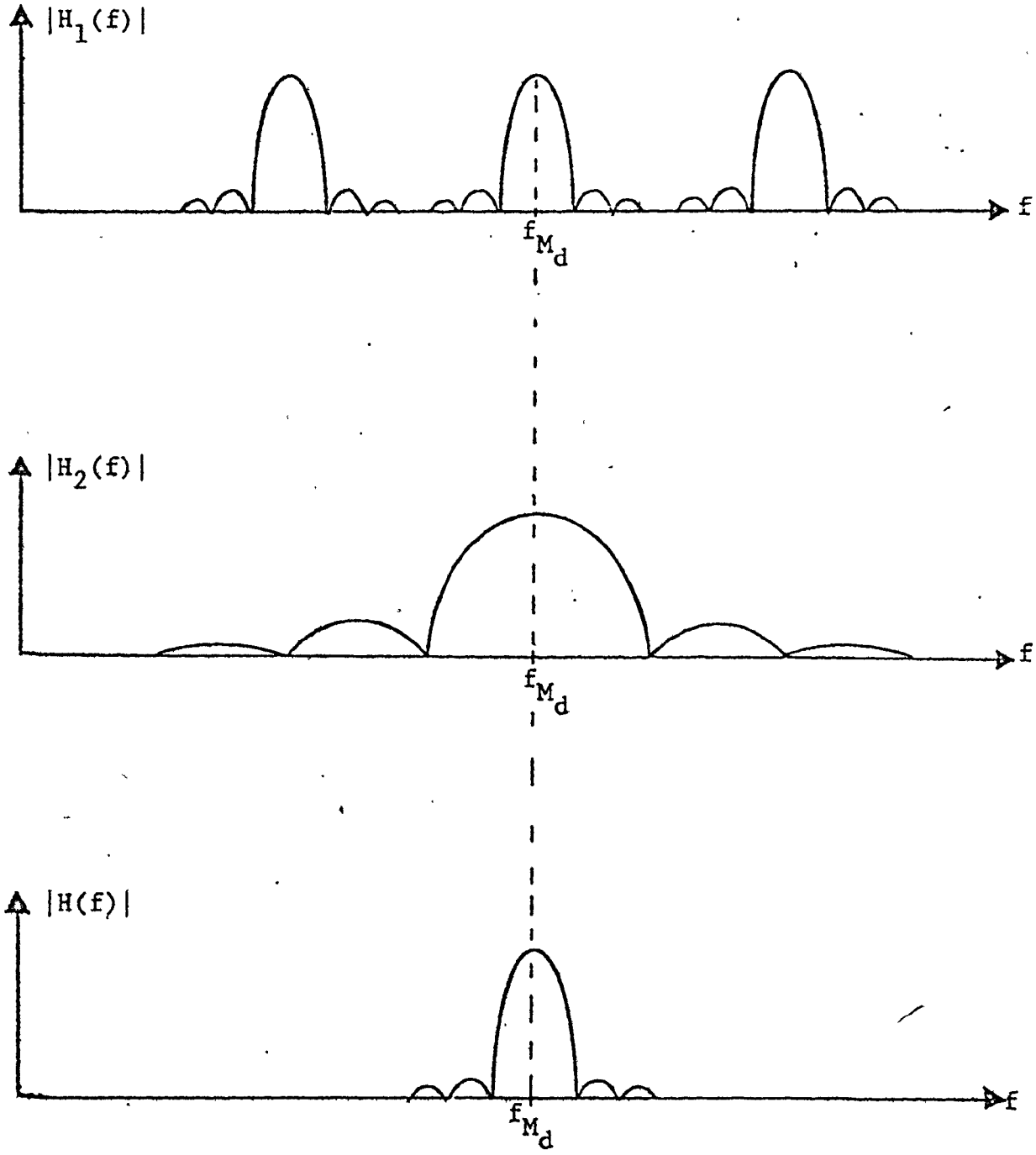

Fig. 4.5 The various transfer functions of the stepped-finger transducer.

CHAPTER V

DESIGN AND FABRICATION OF HARMONIC SAW DELAY LINES

5.1 General

The primary design consideration for SAW delay lines is the choice of the substrate. Other design considerations such as finger width, frequency stability and amplitude levels all depend on the choice of the substrate. Figure 5.1 [23] shows the most commonly used piezoelectric substrate materials and their general properties. Examination of these properties show that lithium niobate ($LiNbO_3$) has the highest coupling coefficient, k^2, which is a measure of the efficiency with which electrical energy is converted into mechanical energy on a piezoelectric substrate. The delay lines reported in this thesis used $LiNbO_3$ substrates, though delay lines were made using quartz substrates as well. The results obtained from the delay lines built on quartz were similar to the results obtained from the delay lines built on $LiNbO_3$, except that the delay lines built on quartz had higher insertion losses as predicted by the lower k^2 value of quartz.

Material	Orientation	v_a m/s	$\frac{\Delta v_a}{v_\infty}$	k^2 (measured)	Temperature Coeff. of Delay ppm/°C	C_{FF_d} in F/m for $\frac{d}{L} = 0.5$	Attenuation at 1 GHz dB/μsec in Air	T τ_{PR}
$LiNbO_3$	Y,Z	3488	0.0241	0.045	85	4.6438×10^{-10}	0.88	50.2
$LiNbO_3$	41.5°X	4000	0.028	0.057	67	6.1857×10^{-10}	0.75	67.2
Quartz	Y,X	3159	0.0009	0.0023	-24	5.00664×10^{-11}	2.15	4.52
Quartz	ST,X (Y+42 3/4°,X)	3158	0.0006	0.0016	0	5.03385×10^{-11}	2.62	4.55

Fig. 5.1 The most commonly used piezoelectric substrates and their general properties.

The delay lines reported in this thesis were all made with a metallization ratio, η, of 0.9. This value of η was chosen for two reasons:

(1) at $\eta = 0.9$ the highest number of harmonics are present, so that the delay lines would not have the inherent harmonic filtering which is possible at other metallization ratio values. In this way the internal harmonic filtering ability of each delay line will be due solely to the geometric design; and

(2) at $\eta = 0.9$ all the harmonics are approximately of the same amplitude level for the 2-, 3-, and 4-finger geometries. This condition is necessary for a fair comparison of Kerbel's and Engan's filtering method and the stepped-finger filtering method.

In this chapter the design procedures for building a delay line operating at a higher harmonic mode and exhibiting internal filtering of unwanted modes will be outlined for Kerbel's and Engan's method and the stepped-finger method. The steps necessary for the fabrication of these delay lines will also be stated.

5.2 Kerbel's and Engan's Harmonic Delay Line Design

The delay line was chosen to operate at a higher harmonic frequency of 114.4 MHz. The 3-finger input

transducer was chosen to have its 5th harmonic frequency coincide with the operating frequency of 114.4 MHz. Therefore for the 3-finger transducer, its fundamental frequency:

$$f_o = \frac{114.4}{5} = 22.88 \text{ MHz}$$

and its fundamental wavelength:

$$\lambda_o = \frac{\nu}{f_o} \tag{5.1}$$

$$= \frac{3488}{22.88 \times 10^6}$$

$$= 1.52 \times 10^{-4} \text{ m.}$$

$$= 0.006 \text{ inches}$$

For the 3-finger geometry, the sum of the finger width, X, and the gap width, Y:

$$X + Y = \frac{\lambda_o}{3} \tag{5.2}$$

also

$$\frac{X}{X+Y} = 0.9 \quad \text{for } \eta = 0.9$$

or $X = 9Y$ (5.3)

From equations (5.2) and (5.3), we get:

$$Y = \frac{\lambda_o}{30} \tag{5.4}$$

$$= 2.0X10^{-3} \text{ inches}$$

and

$$X = 9\,\frac{\lambda_o}{30} = 0.3\lambda_o \tag{5.5}$$

$$= 1.8X10^{-3} \text{ inches}$$

From [24] and [25] for a 3-finger transducer at $\eta = 0.9$, the capacitance per meter per finger pair:

$$C_{FF} = 1007.71 \text{ pF/m}$$

For minimum untuned insertion loss [26] and [7], the input transducer capacitive susceptance must be made equal to the admittance of the source. For a 50Ω source:

$$\left|2\pi f_5 C_{T1}\right| = \frac{1}{50} \tag{5.6}$$

where C_{T1} is the total capacitance for the input transducer. Thus from equation (5.6):

$$C_{T1} = \frac{1}{2\pi(50)(114.4X10^{6})}$$

$$= 27.82 \text{ pF}$$

The total number of fingers in the input transducer was chosen to be 30, thus the aperture width:

$$W = \frac{2C_{T1}}{C_{FF}N_1} \tag{5.7}$$

$$= 5.68X10^{-2} \text{ inches}$$

The specifications for the design of the 3-finger input transducer is now complete.

The 4-finger output transducer was chosen to have its 11th harmonic frequency coincide with the operating frequency of 114.4 MHz. Thus the fundamental frequency for the 4-finger transducer:

$$f_o = \frac{114.4}{11} = 10.4 \text{ MHz}$$

and the fundamental wavelength from equation (5.1):

$$\lambda_o = \frac{3488}{10.4X10^{6}} \text{ m}$$

$= 1.32X10^{-2}$ inches

For the 4-finger geometry, the sum of the finger width, X, and the gap width, Y:

$$X + Y = \frac{\lambda_o}{4} \tag{5.8}$$

and

$$X = 9Y \quad \text{for } \eta = 0.9 \tag{5.9}$$

From equations (5.8) and (5.9), we get:

$$Y = \frac{\lambda_o}{40} \tag{5.10}$$

$= 3.3X10^{-4}$ inches

and

$$X = 0.225\lambda_o \tag{5.11}$$

$= 2.97X10^{-3}$ inches

From [24] and [25] for a 4-finger transducer at $\eta = 0.9$, the capacitance per meter per finger pair:

$C_{FF} = 1488.38$ pF/m

The output transducer consisted of 12 fingers and had the same aperture width as the input transducer, therefore the output transducer capacitance:

$$C_{T2} = \tfrac{1}{2}C_{FF}N_2W \qquad (5.12)$$

$$= 12.89 \text{ pF} \quad \text{for } N_2 = 12$$

A picture of the completed 3- and 4-finger delay line is shown in Figure 5.2.

5.3 Stepped-Finger Harmonic Delay Line Design

For comparison purposes this delay line was also chosen to operate at a harmonic frequency of 114.4 MHz. The 5th harmonic frequency was chosen to be the desired harmonic mode (i.e. $M_d = 5$). Therefore the fundamental frequency:

$$f_o = \frac{114.4}{M_d} \text{ MHz}$$

$$= 22.88 \text{ MHz}$$

and the fundamental wavelength from equation (5.1):

$$\lambda_o = \frac{3488}{22.88X10^6}$$

$$= 1.52X10^{-4} \text{ m}$$

$$= 0.006 \text{ inches}$$

Fig. 5.2 Picture of the 3- and 4-finger delay line operating at 114.4 MHz.

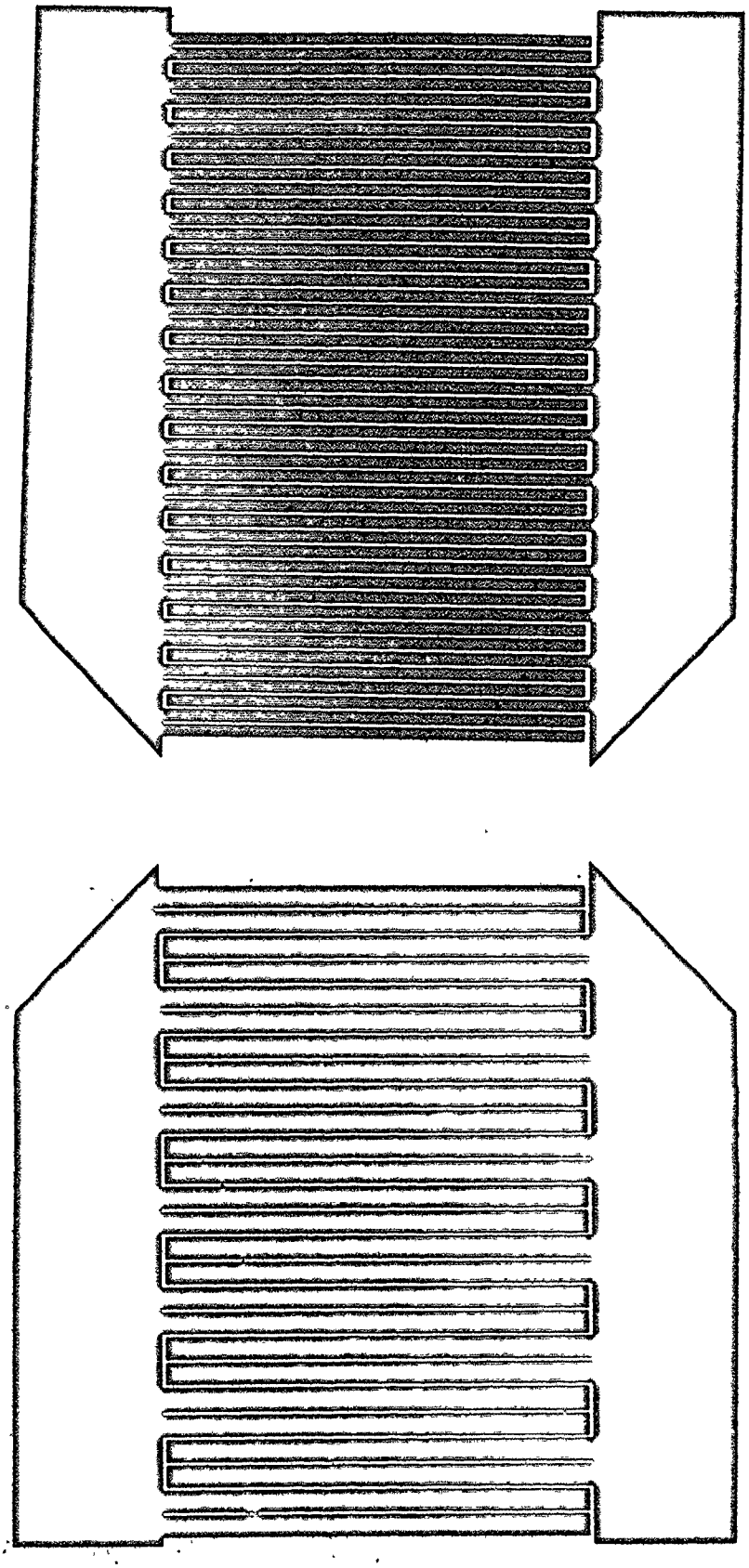

Since the transducers of this delay line are of the 2-finger geometry, the sum of the finger width, X, and the gap width, Y:

$$X + Y = \frac{\lambda_o}{2} \tag{5.13}$$

For a metallization ratio of 0.9:

$$\frac{X}{X+Y} = 0.9$$

$$X = 9Y \tag{5.14}$$

From equations (5.13) and (5.14)

$$Y = \frac{\lambda_o}{20} \tag{5.15}$$

$$= 3.0X10^{-4} \text{ inches}$$

and

$$X = 0.45\lambda_o \tag{5.16}$$

$$= 2.7X10^{-2} \text{ inches}$$

From [24] and [25] for a 2-finger transducer at $\eta = 0.9$, the capacitance per meter per finger pair:

$$C_{FF} = 920 \text{ pF/m}$$

The input transducer capacitive susceptance for a 50Ω source from equation (5.6):

$$C_{T1} = 27.82 \text{ pF}$$

Making the total number of fingers in this input transducer also equal to 30, from equation (5.7) the aperture width:

$$W = 0.079 \text{ inches} \quad \text{for } N_1 = 30$$

Since the desired harmonic mode is the 5th, from the theory of the stepped-finger transducer outlined in Chapter IV, each finger must be divided into 5 equal segments, making the width of each segment:

$$W_s = \frac{W}{M_d} \tag{5.17}$$

$$= 0.016 \text{ inches}$$

and each segment must be displaced from its neighbour by:

$$\frac{\lambda_o}{M_d} = 1.2\text{X}10^{-3} \text{ inches}$$

Making the total number of fingers in the output transducer equal 12, gives the output capacitance from equation (5.12):

C_{T2} = 11.13 pF for N_2 = 12

A picture of the completed stepped-finger delay line is shown in Figure 5.3.

5.4 Fabrication of Delay Lines

The techniques and equipment used for making SAW devices are very much similar to those of electronic semiconductor devices. The most common fabrication techniques [27] are photolithography, image projection and electron beam lithography.

The photolithography method uses a contact mask for the formation of the photoresist circuit pattern onto the substrate. The mask may be of the non-conformable or conformable kind. The ordinary non-conformable contact mask is only capable of reproducing patterns with minimum line widths of 4 microns. The conformable contact masks are made of very thin glass plates, so that very close contact is achieved when the space between the substrate and mask is evacuated.

Contact masks are not used in the electron beam and image projection techniques. These two methods are used to obtain line widths in the submicron region. The problem with these techniques is that the field of view over which accurate resolution can be obtained is limited, so very

Fig. 5.3 Picture of the Stepped-Finger Delay Line Operating at its 5th Harmonic Mode.

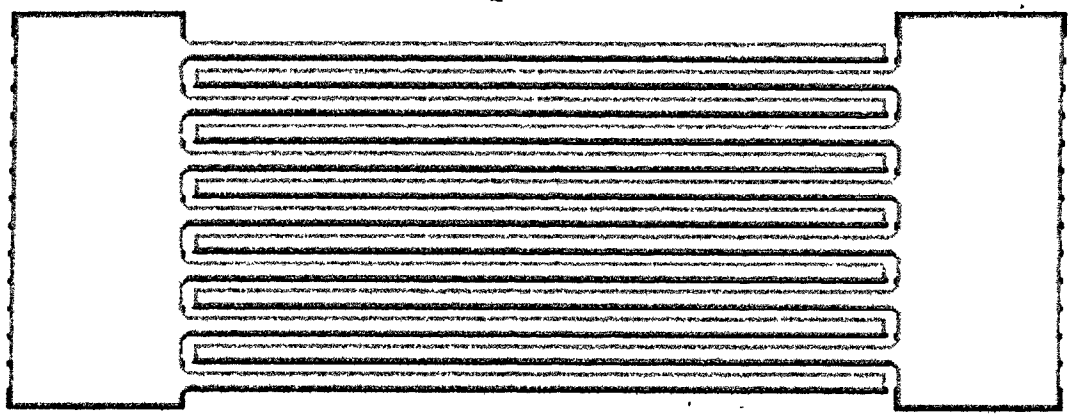

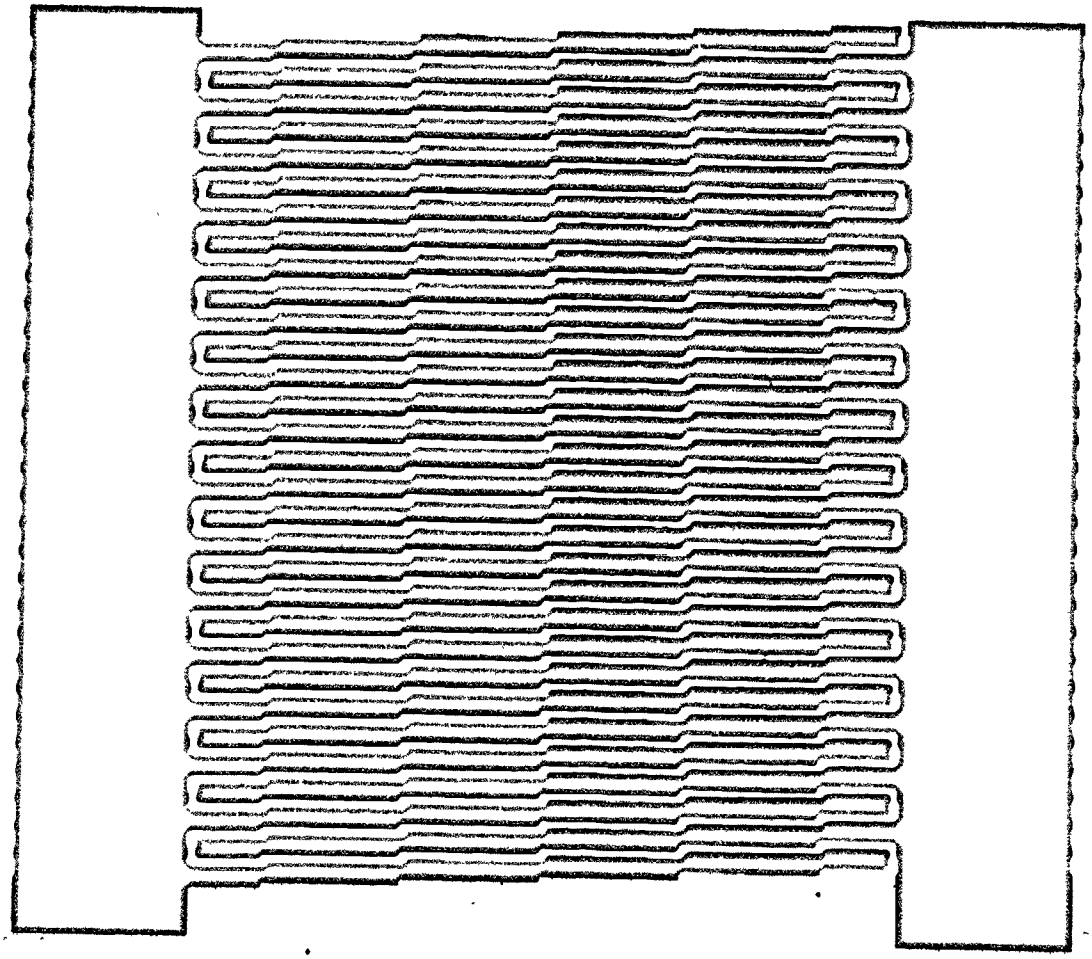

precise step-and-repeat mechanism is required if the pattern exceeds the field of view which is usually the case for SAW devices.

After the photoresist pattern is formed on the substrate, the final metallic pattern can be obtained by chemical etching or lift-off techniques. Chemical etching is used for producing line widths greater than 4 microns, and the lift-off technique for producing line widths in the submicron region.

The delay-lines made for this study had a minimum line width of 5 microns, so the photolithographic technique using non-conformable masks and chemical etching was employed. Each delay line was made using the following four steps:

5.4.1 Artwork and Mask Generation.

5.4.2 Substrate Preparation and Metal Deposition.

5.4.3 Circuit Pattern Transfer to Substrate.

5.4.4 Wiring and Mounting of Device.

5.4.1 Artwork and Mask Generation

The delay line circuit dimensions, as specified in sections 5.2 and 5.3, were first scaled upwards by a factor of 100. These dimensions were then used to cut an enlarged positive pattern of the delay line on red rubylith (Ulano #Q7261), using a Haag Streit AG 1200X1200 mm cutting table. A picture of the table and enlarged rubylith patterns are shown in Figure 5.4.

Fig. 5.4 Picture of rubylith delay line pattern on cutting table.

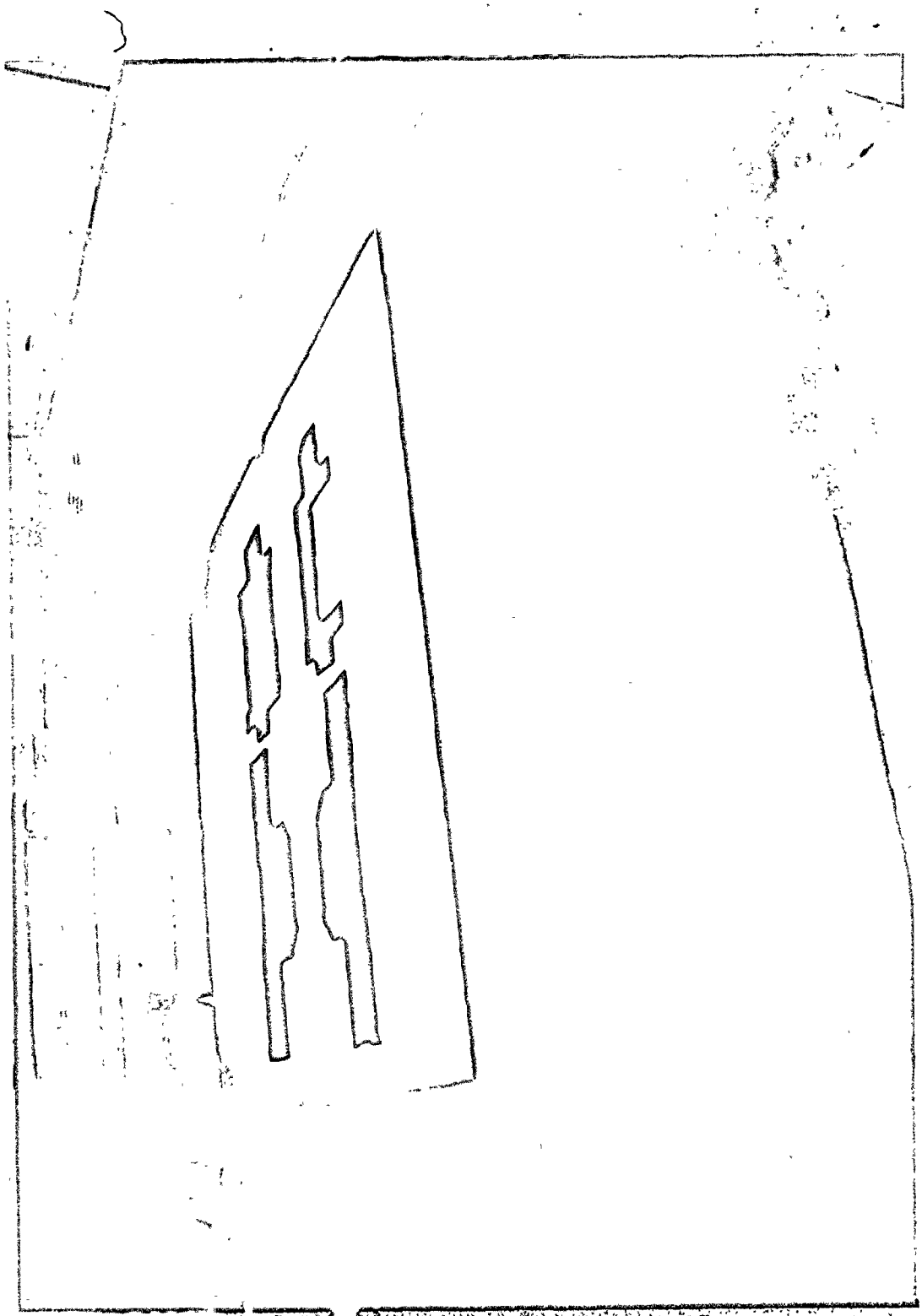

The rubylith patterns were photoreduced by a factor of 5 using a Schneider Repro-Claron camera. The resulting nagatives on 5" X 7" Kodak high resolution film were further reduced by a factor of 20 on a Microkon 1700 camera, which produced the final positive masks on 2" X 2" X 0.06" high resolution Kodak plates.

5.4.2 Substrate Preparation and Metal Deposition

Dust and any other contamination of the substrate surface, onto which the thin metallic film is to be deposited, could result in serious degradation of performance as well as poor adherence of the thin film to the surface. So, before depositing the metallic film, the surface of the substrate has to be thoroughly cleaned.

The substrate is first cleaned in sodium hydroxide solution to remove residual aluminum from any previous deposition. The substrate was then scrubbed with trichloroethylene using cotton swabs for two minutes to remove any oil and grease. Any residual photoresist was then removed by scrubbing with acetone for two minutes. The substrate was then rinsed in distilled water and methanol, and placed to dry in an oven at 85°C for 15 minutes. After drying the substrate was inspected under a microscope for surface contamination. If the substrate was acceptably clean, then it was placed in an Edwards Model 12E3/1670 High Vacuum Coating Unit, and ionic cleaned

using argon gas for 15 minutes.

The vacuum chamber was then evacuated to a pressure of approximately 10^{-5} torr (mm Hg), and 1000 Å to 2000 Å of 99.99% pure aluminum was evaporated onto the substrate. The deposition rate was not critical since aluminum adheres well to lithium niobate. The substrate was left to cool in the chamber for 4 hours before being removed for circuit pattern transfer. A picture of the coating unit is shown in Figure 5.5.

5.4.3 Circuit Pattern Transfer to Substrate

The metallized substrate was placed on the vacuum chuck of the Headway spinner, and rinsed with methanol, then spun dry at 6000 rpm for two minutes.

The metallized surface was then covered with filtered Shipley AZ-1350B positive photo resist, and spun at 6000 rpm for two minutes. The substrate was then pre-baked for 15 minutes at 80°C.

After pre-baking, the substrate was mounted on the wafer vacuum chuck of the Kasper Model 2001 Alignment machine. The glass mask, containing the positive image of the delay line circuit, was mounted on the mask holder. The mask was then carefully aligned with the substrate using the "Row and Column", "Low Power Split Field" and the "High Power Split Field" positions of the aligner. The mask and substrate

Fig. 5.5 Picture of Edwards High Vacuum Coating Unit.

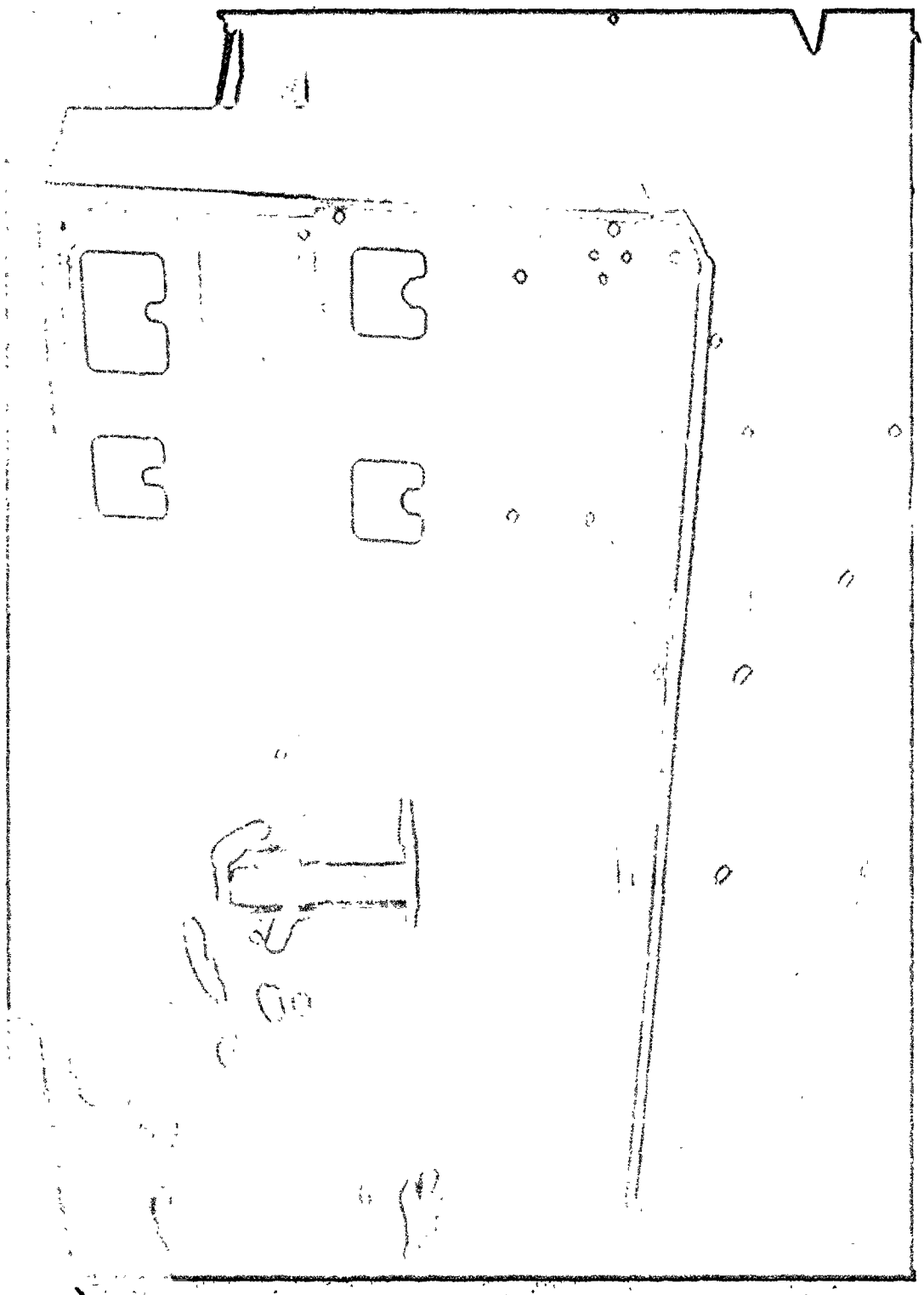

were then exposed for five seconds to ultraviolet light of intensity 4 mW/cm^2. A picture of the alignment machine in shown in Figure 5.6.

The exposed substrate was developed in AZ-1350 Shipley developer until all the exposed photoresist had been dissolved. The substrate was then rinsed with distilled water and placed in an acid etch composed of phosphoric, acetic and nitric acids in volumetric ratio 25:5:1. To prevent excessive undercutting the etching process was observed under a microscope. After all the exposed aluminum had dissolved, the substrate was removed from the etchant and rinsed with distilled water. Unexposed photoresist was then removed with acetone. The substrate was now ready for packaging and wiring if the etched pattern was acceptable.

5.4.4 Wiring and Mounting of Device

The substrate was glued to a 2¼" X 2¼" X ½" aluminum box using Apiezon sealing wax. Apiezon vacuum grease was placed at the edges of the substrate to prevent reflection of the acoustic waves from the edges. The bus bars of the transducers were connected to the OSM type connectors used for input and output ports on the aluminum box, via 0.001" diameter, 99.99% gold wires. The connections were made using GC Silver Conductive Paint. Pictures of the two delay lines mounted and wired to aluminum boxes are shown in Figures 5.7 and 5.8.

Fig. 5.6 Picture of Kasper Model 2001 Alignment Machine.

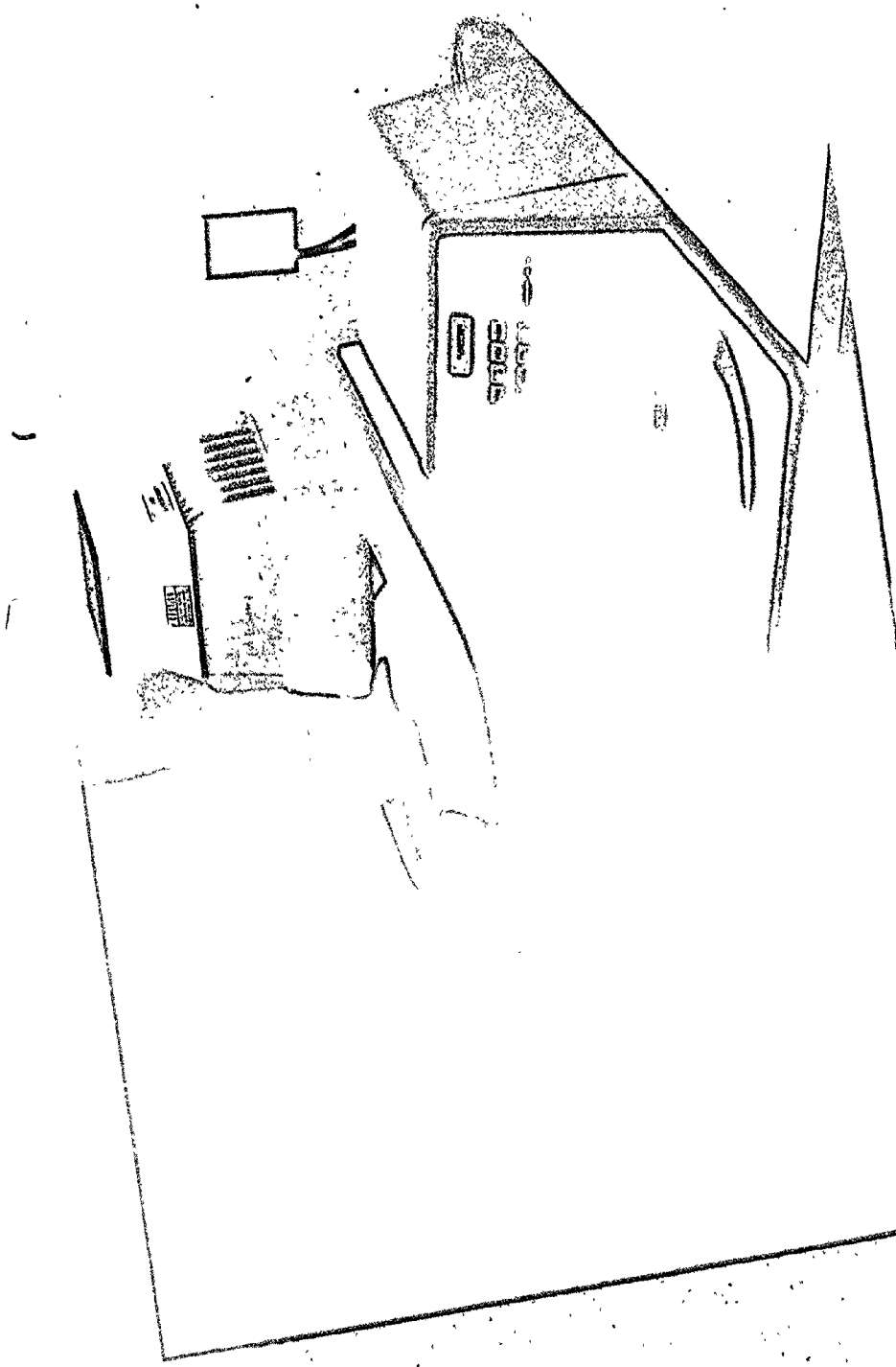

Fig. 5.7 Picture of Kerbel and Engan Delay Line Mounted and Wired in an Aluminum Case.

Fig. 5.8 Picture of Stepped-Finger Delay Line Mounted and Wired in an Aluminum Case.

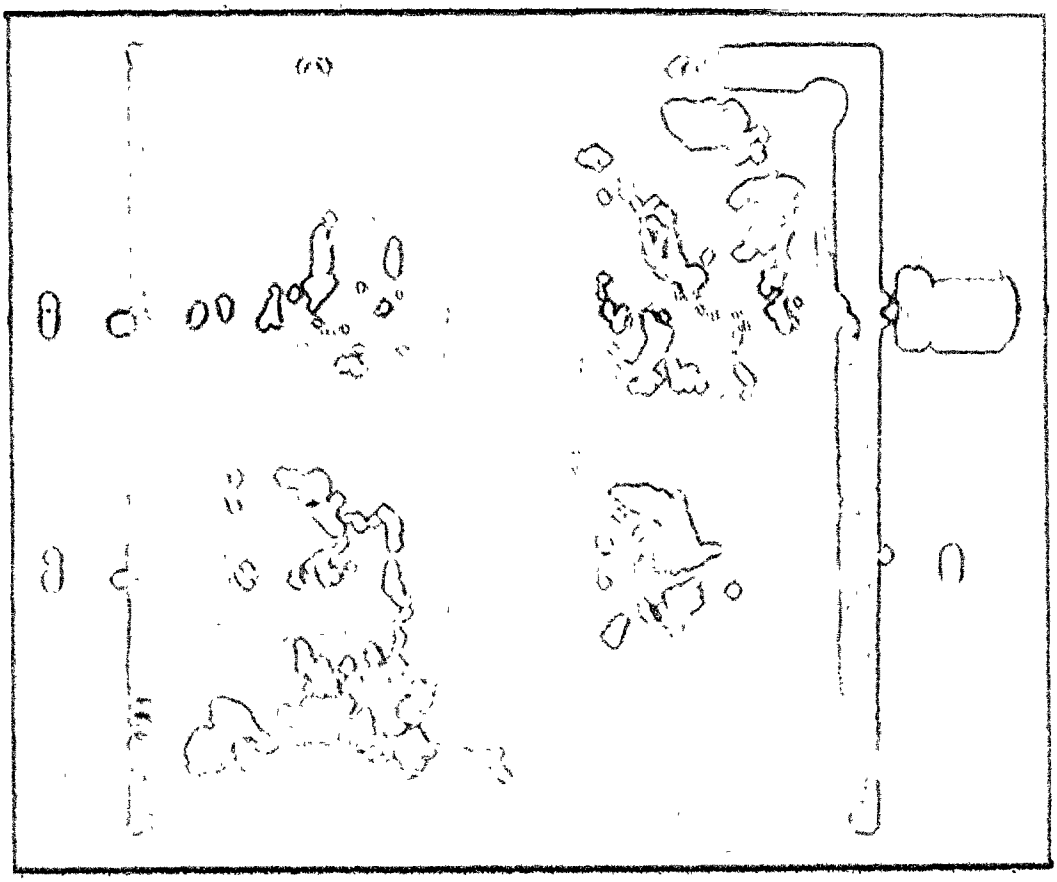

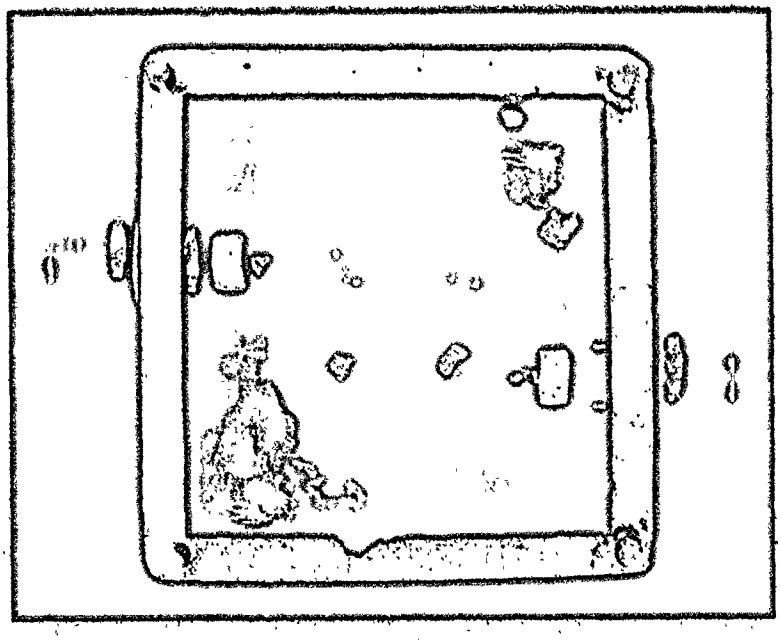

CHAPTER VI

EXPERIMENTAL RESULTS

6.1 General

The two delay lines specified and fabricated as outlined in Chapter V were individually tested and compared. Particular emphasis was placed on the amplitude response of both delay lines. The ability of the delay lines to efficiently generate the desired harmonic mode and attenuate the undesired modes was measured by noting the insertion losses at those harmonic frequencies.

6.2 Instrumentation

The amplitude responses of the delay lines were measured using a Singer Alfred Sweep Oscillator 6600 and a Singer Alfred Sweep Network Analyser 8000/7051. A Systron Donner Frequency Counter 6243A was used along with the internal markers of the Singer Alfred Sweep Oscillator to make precise frequency measurements. A connection diagram of the entire testing instrumentation is shown in Figure 6.1.

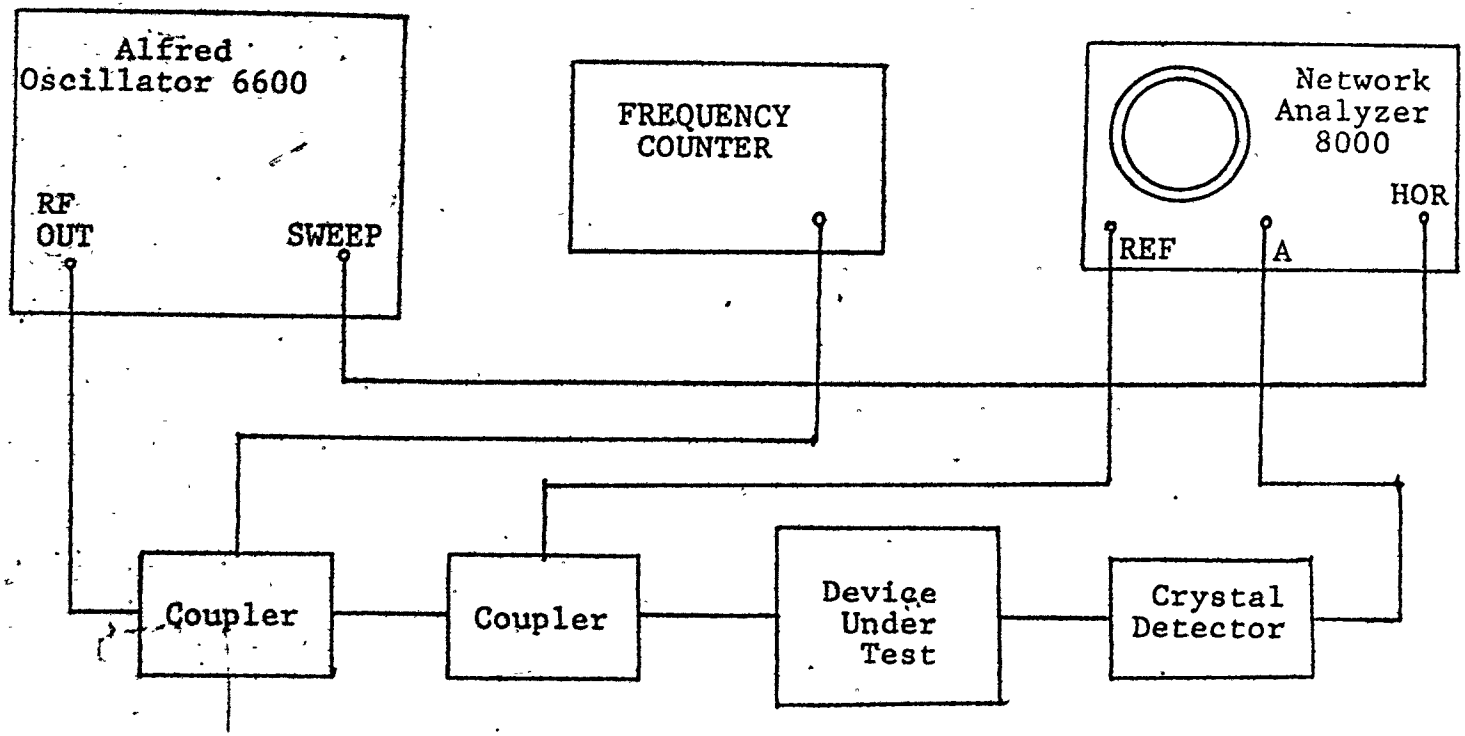

Fig. 6.1 Connection diagram of the test instrument used for measuring the amplitude responses of the delay lines.

All measurements were done with the frequency range switch of the frequency generator in the 0.01 - 1 GHz position. The RF output of the generator was split twice using two Merrimac Couplers CRM-15-500. One portion of the splitted RF signal was applied to the Reference Channel of the network analyser, another portion to the frequency counter and another portion to the input port of the delay line under test. The resulting signal coming out of the output port of the delay line was applied to Channel A of the network analyser via an Alfred Model 1403 crystal detector. All connections were made using 50Ω coaxial cable. A photograph of the instrumentation is shown in Figure 6.2.

The input and output capacitance of the delay lines were also measured using a General Radio Capacitance Bridge 1615-A.

6.3 Results

Figure 6.3 shows the experimental frequency response obtained from both delay lines when frequency swept from approximately 17 MHz to 147 MHz. From Figure 6.3(a) it can be seen that the desired harmonic of Kerbel's and Engan's delay line peaks at approximately -23 dB; but from Figure 6.3(b) the desired harmonic of the stepped-finger delay line peaks at approximately -17 dB. These results indicate that the desired harmonic of the stepped delay line has a gain of about 6 dB over the desired harmonic of Kerbel's and Engan's delay line.

Fig. 6.2 Photograph of the Instruments Used for Measuring the Amplitude Responses of the Delay Lines.

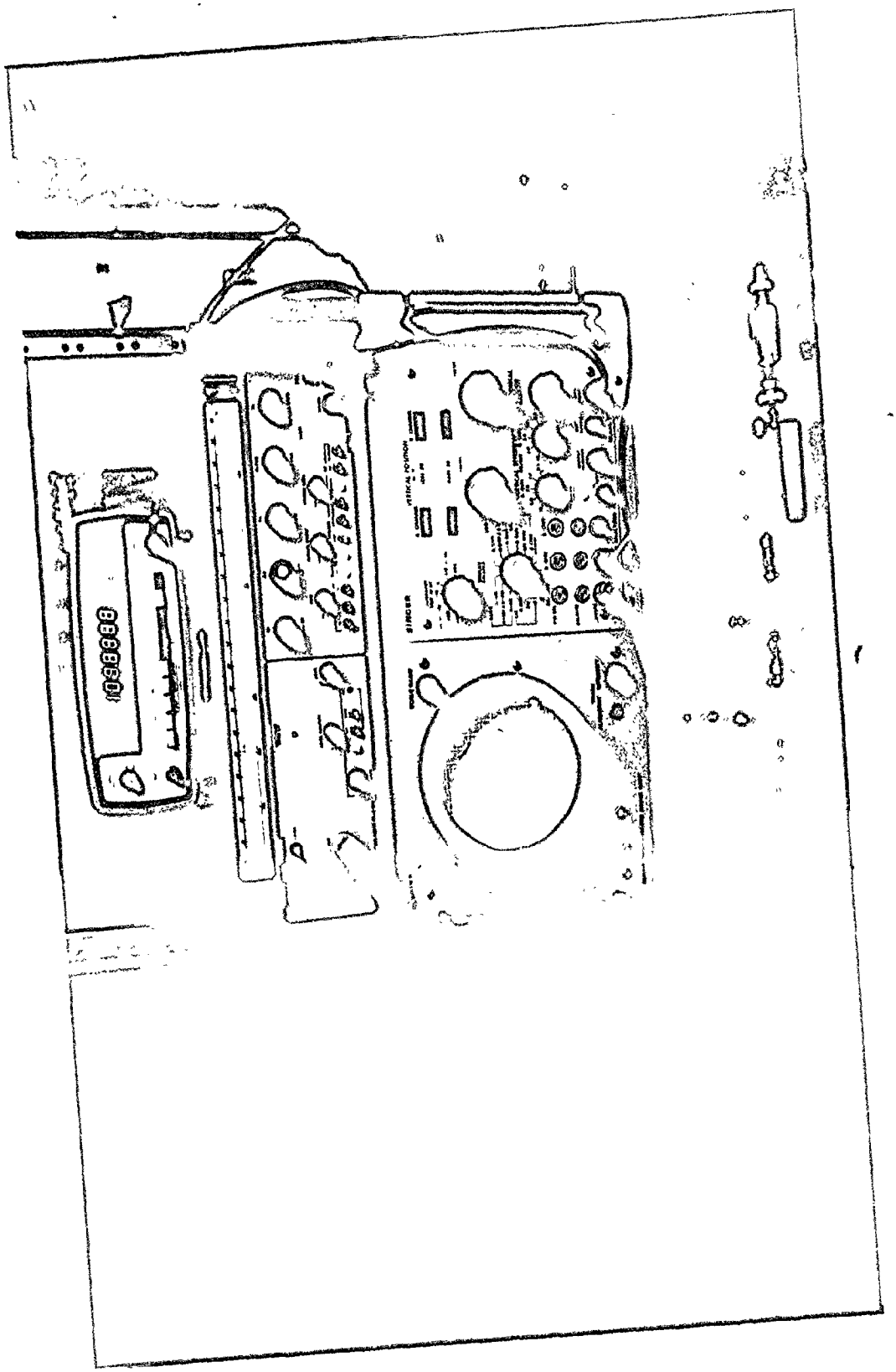

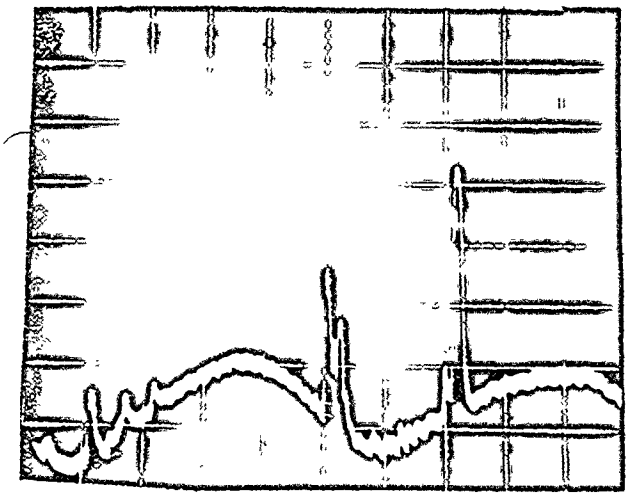

(a) Kerbel and Engan delay line response
Vertical Scale: 5 dB/div.
Horizontal Scale: 13 MHz/div.

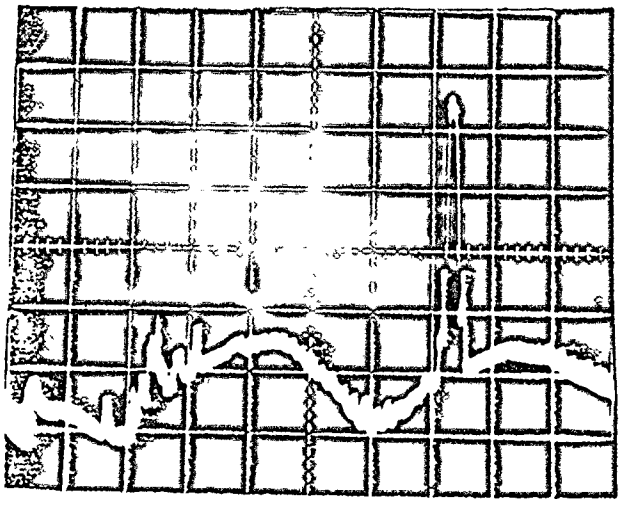

(b) Stepped-finger delay line response
Vertical Scale: 5 dB/div.
Horizontal Scale: 13 MHz/div.

Fig. 6.3 Frequency response of the two delay lines from 17 MHz - 147 MHz.

Figure 6.4 shows the frequency response obtained from the delay lines when frequency swept from approximately 17 MHz to 272 MHz.

Figures 6.3 and 6.4 show the frequency response of all the undesired harmonics below and above the desired harmonic in frequency obtained from the two delay lines. These Figures show that the highest amplitude level of an undesired harmonic is 18 dB below the peak of the desired harmonic for the stepped-finger delay line, and only 9 dB for the Kerbel and Engan delay line. This indicates that the stepped-finger delay line was more successful than the Kerbel and Engan delay line in suppressing the undesired harmonic modes. A summary of the amplitude levels of the desired and undesired harmonic modes is given in Figure 6.5 for both delay lines.

Figure 6.6 gives an expanded view of the frequency response of the two delay lines at the desired harmonic frequency. Note the shift in the actual centre frequency to 112.5 MHz from the calculated value of 114.4 MHz. This represents an error of 1.67% in the centre frequency of the desired harmonic. This error is due to two reasons. First the velocity of the surface wave is reduced from its free surface value (the value used in Sections 5.2 and 5.3 for calculating the finger spacings), because the transducer fingers act as shorts to the piezoelectric fields. Secondly the mass of the metal fingers cause a mass loading effect

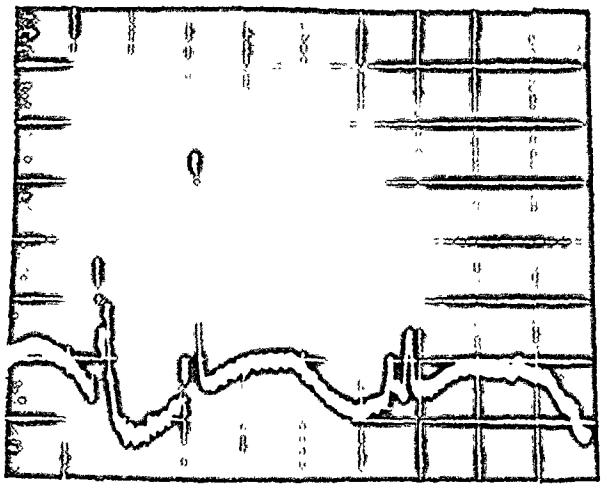

(a) Kerbel and Engan delay line frequency response
Vertical Scale: 5 dB/div.
Horizontal Scale: 25.5 MHz/div.

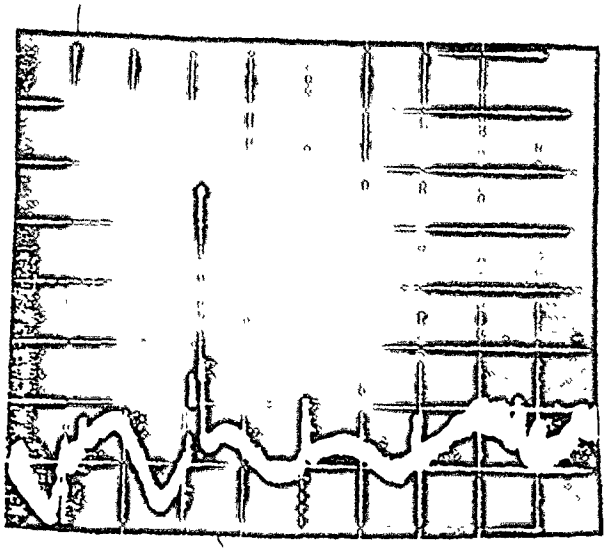

(b) Stepped-finger delay line frequency response
Vertical Scale: 5 dB/div.
Horizontal Scale: 25.5 MHz/div.

Fig. 6.4 Frequency response of the two delay lines from 17 MHz - 272 MHz.

Finger Geometry	Harmonic Mode	Suppression dB
Stepped	Desired	17
3,4	Desired	23
Stepped	Fundamental	43
3	Fundamental	46
4	Fundamental	46
Stepped	3rd	37
3	2nd	42
4	3rd	43
Stepped	7th	35
3	4th	32
4	9th	36
Stepped	9th	36
3	8th	37
4	15th	40

Fig. 6.5 Summary of the amplitude levels of the desired and undesired harmonic modes for the two delay lines.

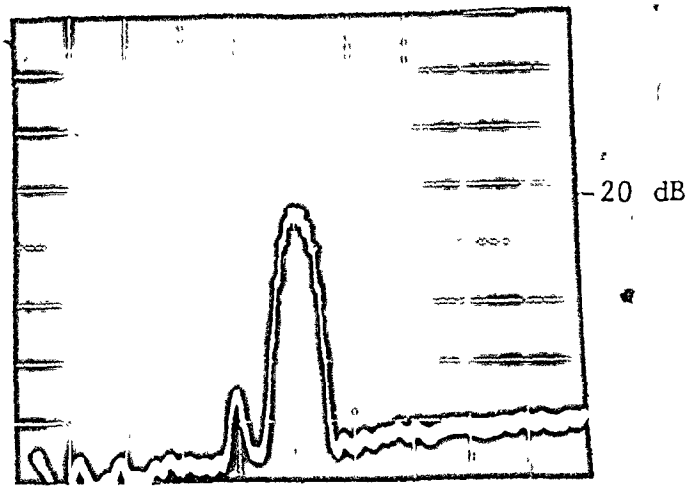

(a) Kerbel and Engan delay line response
Vertical Scale: 5 dB/div.
Horizontal Scale: 3 MHz/div.

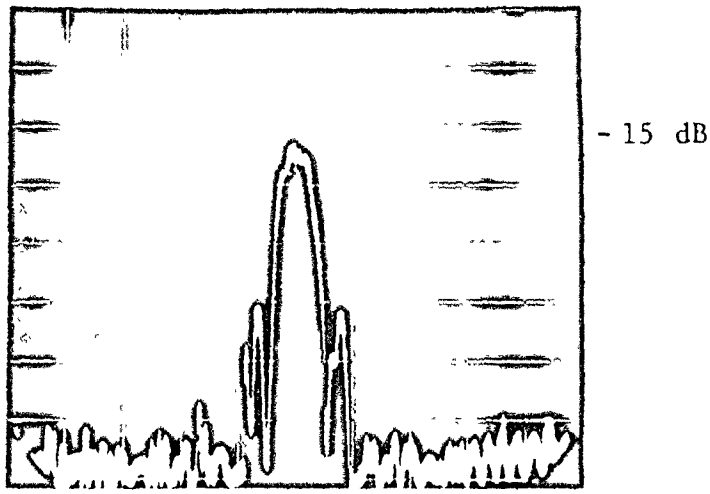

(b) Stepped-finger delay line response
Vertical Scale: 5 dB/div.
Horizontal Scale: 3 MHz/div.

Fig. 6.6 Frequency response of the two delay lines at the desired harmonic mode.

on the surface of the substrate which tends to reduce the surface wave velocity also.

Figure 6.6 also shows the presence of ripples in the pass band of the desired harmonic mode. These ripples are due to Triple Transit Echo (TTE). Methods of reducing TTE effects is beyond the scope of this thesis but can be found in [32].

The input and output capacitance, as measured on the capacitance bridge, for the Kerbel and Engan delay line were:

$$C_{T1} = 29.3 \text{ pF}$$

$$C_{T2} = 13.6 \text{ pF}$$

and for the stepped-finger delay line:

$$C_{T1} = 28.4 \text{ pF}$$

$$C_{T2} = 12.2 \text{ pF}$$

These values were all within 10% of their calculated value. This implies that the aperture widths of both delay lines were of the optimum length for minimum untuned insertion loss.

CHAPTER VII

CONCLUSIONS

7.1 General Conclusions

Two surface acoustic wave delay lines have been designed and built to operate at a higher harmonic mode without any external filtering devices. One of these harmonic delay lines was built using a 3-finger geometry for the input transducer and a 4-finger geometry for the output transducer, a design originally developed by Kerbel [11] and Engan [15]. Although this design works well, its major disadvantage is its reliance on multielectrode transducers which are very difficult to build at high frequencies. The second harmonic delay line, however, can be built using the 2-finger geometry transducer with each finger modified to a step-like shape. This new design was called the stepped-finger delay line.

The experimental results obtained from the two harmonic delay lines clearly show that the stepped-finger delay line is more efficient in generating the desired harmonic mode, since its amplitude level was 6 dB higher than that of the Kerbel and Engan delay line. The results also show that the

stepped-finger delay line is more successful in suppressing all unwanted harmonics.

Using Kerbel's own definition for the Improvement Ratio (IR) of a transducer operating at a higher harmonic mode, as stated in equations (4.1) and (4.2), it can be shown that the IR of a stepped-finger delay line will be 50% greater than the IR of a 3-finger transducer, and 100% greater than the IR of a 4-finger transducer, for the same harmonic number and metallization ratio.

The one disadvantage of the stepped-finger delay line is due to the fact that its stepped-finger design is slightly more complex than the usual straight finger design. As a result, to produce the stepped-finger delay line rubylith pattern took five times the amount of time needed for producing the Kerbel and Engan delay line rubylith pattern.

7.2 Further Considerations

The stepped-finger transducer makes possible a method of phase weighting different sections along a finger hitherto unthought of. With this added flexibility in designing SAW transducers a number of other applications for stepped-finger transducers should be considered.

One such consideration should be for the use of the stepped-finger transducer to produce rectangular band pass filters operating at a higher harmonic mode. The principles

would be the same for the harmonic delay line, except that now the output transducer would be stepped and the input transducer apodized according to the sinc function. Further work would be needed to determine the number of fingers necessary in the input and output transducers, so as not to distort the required rectangular frequency response after it is multiplied in frequency by the stepped-output transducer.

Another important consideration would be for using the stepped-finger transducers to produce unidirectional harmonic delay lines. The author has found that by making the following changes in the stepped-finger design:

1. let the displacement be $\frac{\lambda_o}{2M_d}$ instead of $\frac{\lambda_o}{M_d}$
2. let the number of segments in a finger be M_d+1 instead of M_d
3. let the first and the last segment lengths be equal to $\frac{W}{2M_d}$ instead of $\frac{W}{M_d}$

and by making both the input and output transducers stepped according to the above mentioned changes and as illustrated in Figure 7.1, the resulting wave at any summing point R behind either of the two transducers will be zero at the harmonic mode M_d, while in the forward direction the waves add to $M_d A(f_{M_d})$. This can be theoretically verified from equation (4.3).

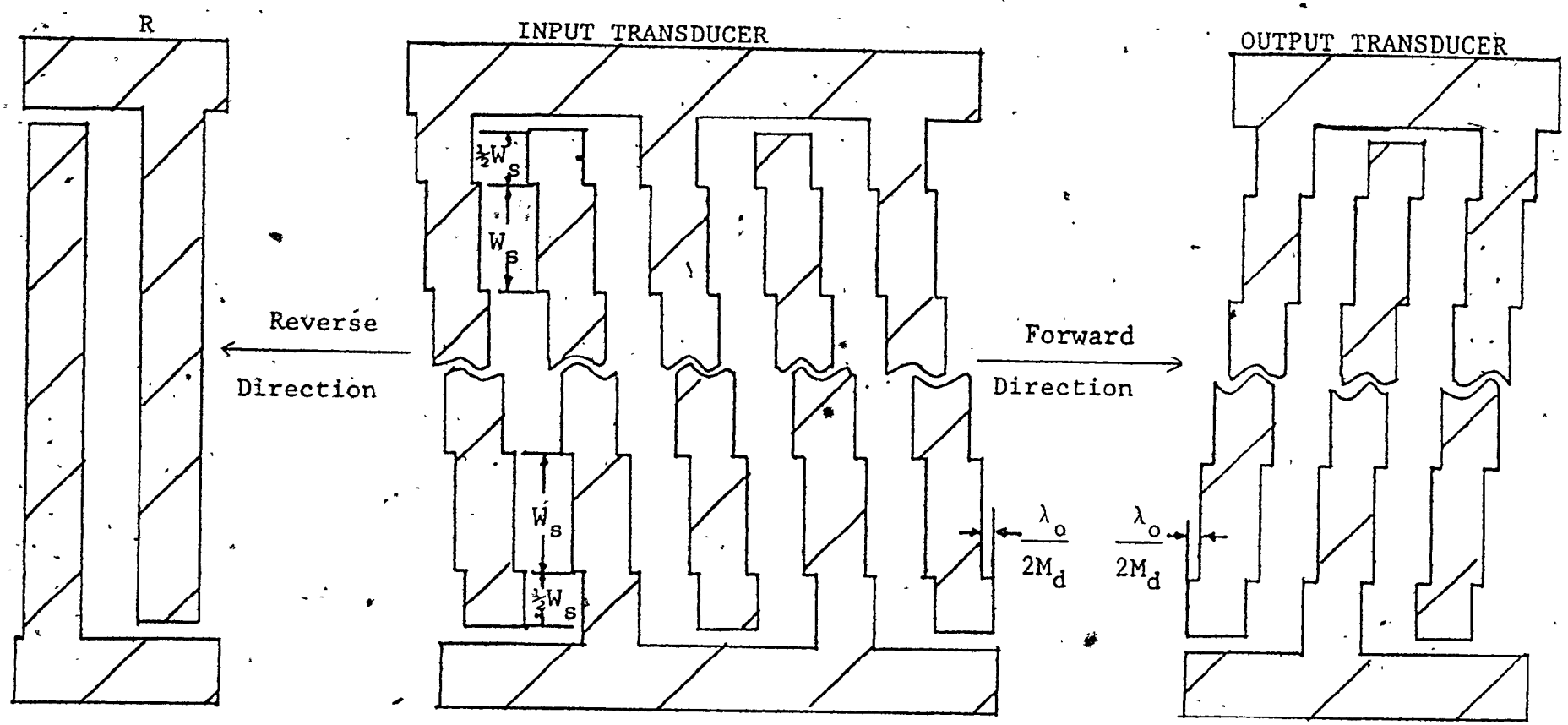

Fig. 7.1 Modified stepped-finger delay line, for adding waves in the reverse direction to zero.

To experimentally verify this fact a stepped-finger delay line was built similar to the one specified in section 5.3, but with both input and output transducers stepped by $\frac{\lambda_o}{10}$ and with 6 segments per finger. Uniform broadband receiving transducers were placed behind each stepped-transducer to ascertain how the waves in the reverse directions were adding. The frequency responses of this delay line in the forward and reverse directions are shown in Figure 7.2. From Figure 7.2(a) it can be seen that at the 5th harmonic mode the waves travelling in the reverse direction add to zero, as is evident from the sharp null at f_5. Figure 7.2(b) verifies that in the forward direction the waves add constructively at f_5.

By dividing a transducer into reflecting and sending groups with a 90 degrees phase shift between the groups, Yamanouchi et. al. [33] were able to make the waves travelling in the reverse direction add to zero and the waves in the forward direction add constructively, at a given fundamental frequency. These group-type delay lines also exhibited unidirectionality.

It is the author's opinion that by combining the group-type structure with the stepped-finger structure a unidirectional delay line could be built that will not only operate at a higher harmonic mode, but would not require the use of an external 90 degrees phase shifter. Further work has to be done to realize this design.

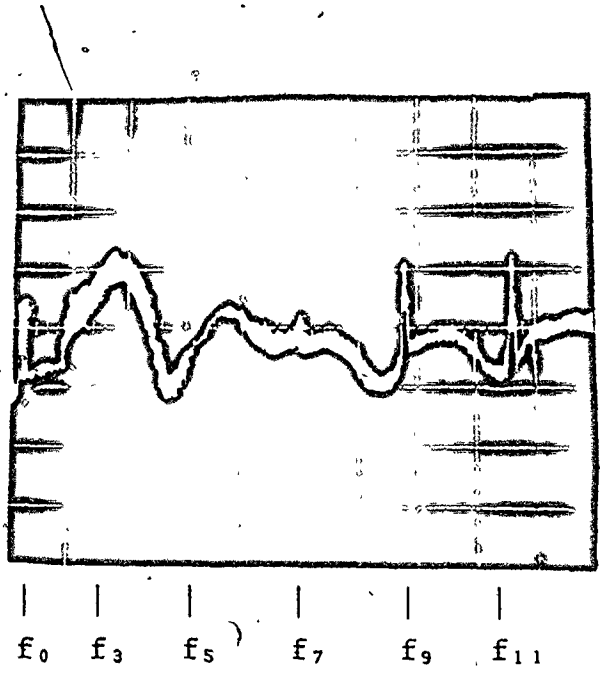

(a) Vertical Scale: 5 dB/div.
Horizontal Scale: 25 MHz/div.

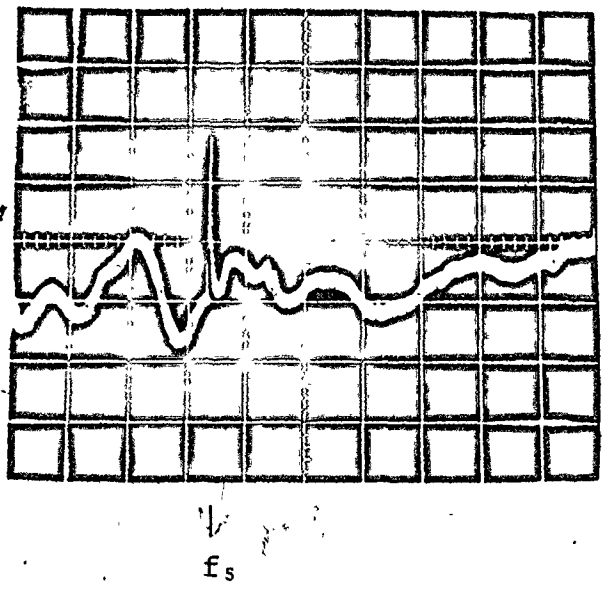

(b) Vertical Scale: 5 dB/div.
Horizontal Scale: 25 MHz/div.

Fig. 7.2 (a) Summation results of waves travelling in the reverse direction.

(b) Summation results of waves travelling in the forward direction.

APPENDIX A

DESIGN AND FABRICATION OF A MULTISTRIP COUPLER FOR USE IN A DELAY LINE OPERATING AT A HARMONIC FREQUENCY

A.1 General

This appendix outlines the theory involved in the design and fabrication of a multistrip coupler used for a twofold purpose. One, for the reduction of undesirable bulk waves and two, for the isolation of a selected harmonic mode.

Two delay lines of metallization ratios of 0.9 were fabricated. The two delay lines were exactly alike except that one of them contained the multistrip coupler between the input and output transducer. Both delay lines were optimized for minimum untuned insertion loss at their 3rd harmonic. The multistrip coupler was designed to give 100 per cent energy transfer at the 3rd harmonic, and to behave as an attenuator at the other harmonic frequencies.

Experimental results are given for both delay lines and a comparison of the results is made.

A.2 Input and Output Transducer Design

The crystal chosen for building these delay lines was lithium niobate ($LiNbO_3$). The general properties of this material are shown in Figure 5.1.

The fundamental frequency (f_o) for the SAW delay lines was chosen to be 22.887 MHz and the metallization ratio 0.9.

The resulting wavelength (λ_o) is thus:

$$\lambda_o = \frac{v}{f} = \frac{3488}{22.887 \times 10^6} = 0.006" \qquad (A.1)$$

For a metallization radio of 0.9:

$$\frac{X}{X+Y} = 0.9 \qquad (A.2)$$

Then for a 2-finger transducer design:

$$X + Y = \frac{\lambda_o}{2} \qquad (A.3)$$

From (A.2) and (A.3), X = 0.0027"

and Y = 0.0003"

The third harmonic frequency, f_3, was chosen as the harmonic mode to be optimized. Since the reactive impedance of the input transducer should equal 50Ω at resonance for a minimum untuned insertion loss [7]:

$$\left|\frac{1}{j2\pi f_3 C_{T1}}\right| = 50 \qquad (A.4)$$

where C_{T1} = static capacitance of input transducer

$$C_{T1} = \frac{1}{2\pi f_3 50} = 46.36 \text{ pF}$$

For $LiNbO_3$ with a metallization ratio of 0.9, the capacitance per meter [24], [25]:

$$C_{FF} = 920 \text{ pF/m}$$

the aperture width:

$$W = \frac{2C_{T1}}{C_{FF}N_1} = 0.132"$$

where N_1 = ~~total~~ number of fingers of input transducer

= 30

Since the output transducer would have the same aperture width, the static capacitance of the output transducer:

$$C_{T2} = C_{FF}WN_2 = 18.54 \text{ pF} \qquad (A.5)$$

where $N_2 = 12$

The transducer design is now complete.

A.3 Multistrip Theory and Design

The Multistrip Coupler (MSC) is an array structure of metal strips deposited on the surface of a piezoelectric substrate as shown in Figure A.1. A surface acoustic wave launched by transducer No. 1 into track A_1, sets up a potential difference between adjacent strips. This potential difference in turn sets up a surface acoustic wave in track A_2.

Modes

A uniform wave generated by transducer No. 1 can be resolved into two modes, the symmetric and antisymmetric modes as shown in Figure A.2. As these two modes travel along the MSC their velocity will be different. This difference in velocity between the two modes will introduce a phase difference:

$$\phi_D = \phi_S - \phi_a = \frac{R_K}{2} k^2 k_f L_M \qquad (A.6)$$

where: ϕ_S = phase of symmetric mode

ϕ_a = phase of antisymmetric mode

R_K = filling factor

k^2 = coupling constant

k_f = wave number

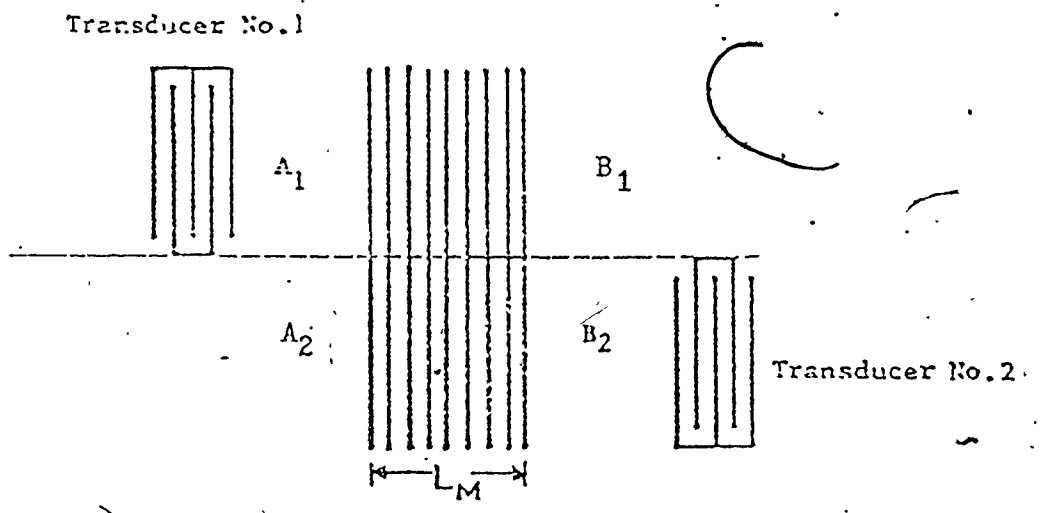

Fig. A.1 Two transducers coupled with a Multistrip Coupler.

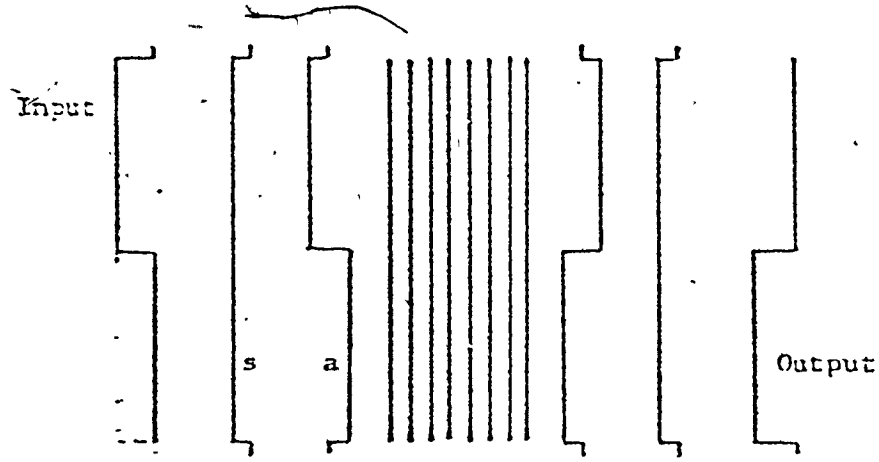

Fig. A.2 The symmetric (s) and the antisymmetric mode (a) of the input and output waveforms.

and L_M = length of MSC

Choosing the Number of Strips, N_T.

If A_1 and A_2 represent complex amplitudes of the input wave on tracks 1 and 2 respectively, and B_1 and B_2 represent the output amplitudes, it can be shown [30] that the matrix relation between them is:

$$\begin{bmatrix} B_1 \\ \\ B_2 \end{bmatrix} = \begin{bmatrix} \cos(\phi_D/2) & -j\sin(\phi_D/2) \\ \\ -j\sin(\phi_D/2) & \cos(\phi_D/2) \end{bmatrix} \begin{bmatrix} A_1 \\ \\ A_2 \end{bmatrix} \qquad (A.7)$$

From (A.7) it can be shown that for a 100% transfer of energy from A_1 to B_2, the phase difference (ϕ_D) must be equal to 180%. This phase difference is directly porportional to the number of strips of the MSC. From (A.6) for a phase difference of π:

$$L_{M\pi} = \frac{\lambda}{R_K k^2} \qquad (A.8)$$

Therefore for a minimum value of $L_{M\pi}$ the value of the filling factor R_K must be a maximum since k^2 and λ are fixed. Values of R_K are plotted in Figure A.3(a) vs. the reciprocol

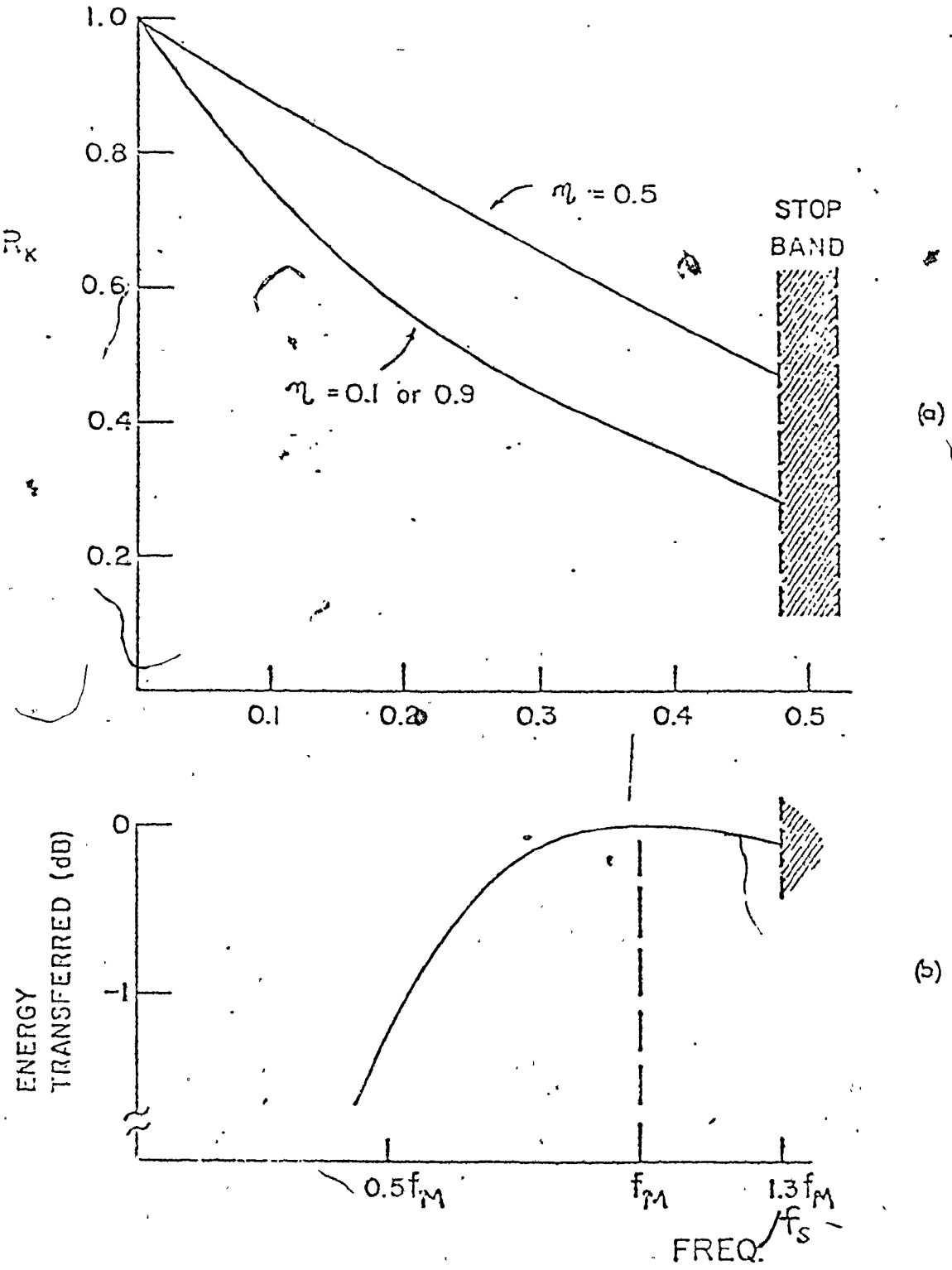

Fig. A.3 (a) Coupling Factor R_K as a function of the number of periods per wavelength, γ.

(b) Theoretical frequency response of a track changer designed for complete energy transfer at $\gamma = 0.375$.

of the number of strips per wavelength, γ. It can be seen that for a metallization ratio of 0.5, R_K is maximum. From Figure A.3(b) it can be seen that for $\gamma = 0.375$ any signal at frequency f_M is transferred without loss, and a stop band is introduced at $f_s = 1.3\ f_M$.

For this design γ was chosen at 0.375 and the metallization ratio at 0.5. The corresponding value of R_K from Figure A.3(a) is 0.58. Substituting this value of R_K into (A.8) with $k^2 = 0.045$ (for $LiNbO_3$):

$$L_{M\pi} \simeq 38\lambda \qquad \text{(A.9)}$$

Therefore the total number of strips in the MSC:

$$N_T = \frac{L_{M\pi}}{\gamma} = 102 \text{ strips}$$

Calculating f_M and the Strip Width

Since the 3rd harmonic was to be isolated and completely transferred:

$$f_M = 3f_o = 68.66 \text{ MHz} \qquad \text{(A.10)}$$

Hence the synchronous frequency of the MSC:

$$f_s = 1.3 \text{ X } f_M = 89.26 \text{ MHz}$$

$$\lambda = \frac{v}{f_s} = 39.1\mu m$$

For a metallization ratio of $\eta = 0.5$:

the strip width $= \frac{\lambda}{4} = 9.77\mu m = 0.0004"$

and the width of the MSC itself:

W_M = 2 X width of transducer = 2 X/U = 0.1534"

This completes the design of the MSC. Both delay lines, one with and one without the MSC, were fabricated using the same procedures as outlined in section 5.4.

Figure A.4 shows a picture of the transducers and the MSC rubylith patterns.

A picture of the completed delay line with the MSC is shown in Figure A.5.

A.4 Experimental Results

Measurements of the amplitude response of the two delay lines were done on a Singer Alfred Sweep Oscillator 6600 and a Singer Alfred Sweep Network Analyzer 8000/705 set on the 0.01 - 1.0 GHz frequency range.

For this discussion the delay line without the multistrip coupler will be referred to as delay line #1, and the delay line with the multistrip coupler will be referred to as delay line #2.

Fig. A.4 Picture of the rubylith patterns of the input and output transducers separated by the multistrip coupler.

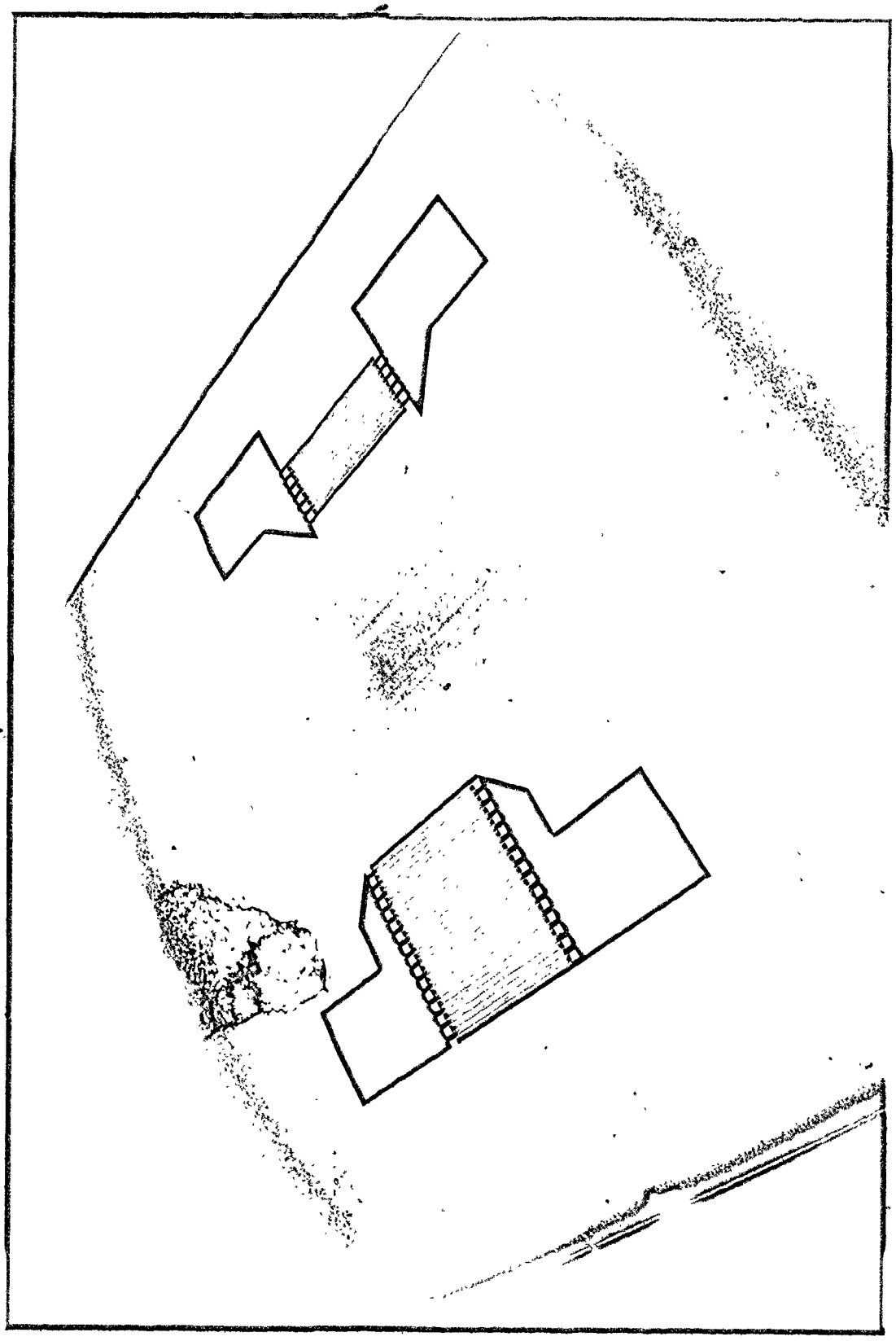

Fig. A.5 Picture of the completed delay line with the MSC mounted in an aluminum case.

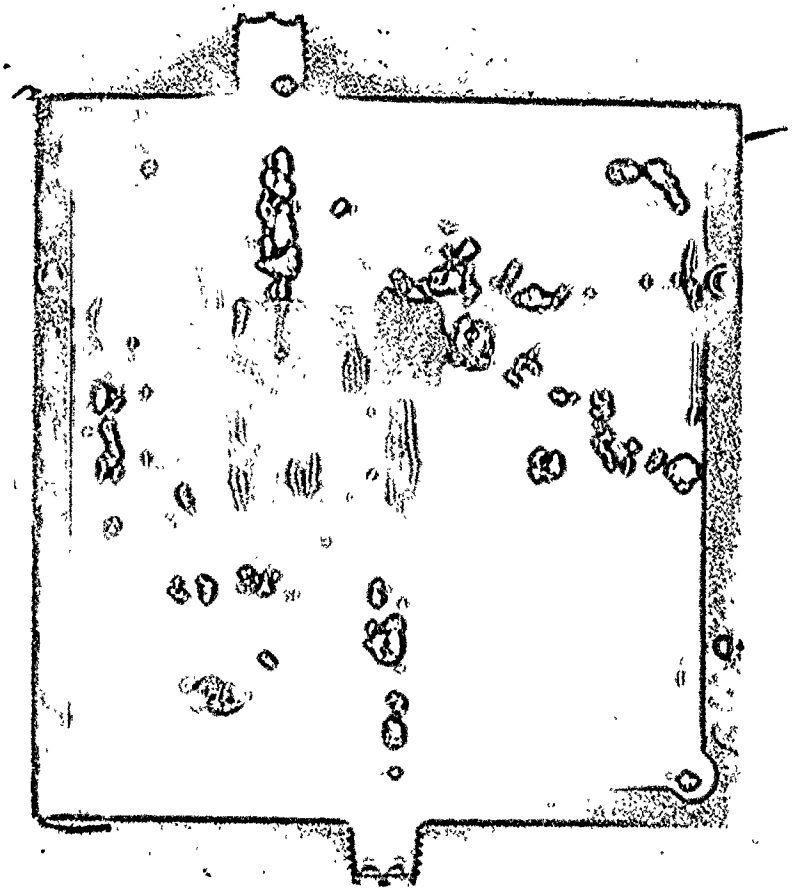

Figure A.6(a) shows the frequency response of delay line #1 from 0 - 350 MHz. As expected for $\eta = 0.9$ all the higher order, odd numbered harmonics are excited up to the 15th (f_{15}) mode. Note also the amount of spurious signals present, and bulk waves response between f_0 and f_3 and between f_5 and f_7. Figure A.6(b) shows the frequency response of delay line #2 from 0 - 350 MHz. As theoretically predicted the multistrip coupler was able to give 100% energy transfer at the 3rd harmonic, and almost completely suppress the bulk waves and spurious signals. Note also the total suppression of the 9th, 13th and 15th harmonic modes. The fundamental, 5th and 7th harmonic modes are also suppressed but not completely since they lie within the pass band of the multistrip coupler.

Figure A.7 gives a more detailed picture of the bulk waves and spurious suppression.

Figure A.8 gives a detailed picture of the 3rd harmonic response. Note the reduction of the sidelobes level from -32 dB to -56 dB attained through the use of the multistrip coupler.

Finally Figure A.9(a) shows the presence of ripples in the pass band due to triple transit reflections at the 3rd harmonic mode. These ripples are almost completely absent in Figure A.9(b). This tends to indicate that the use of a MSC along with absorbing wax acting as reflectionless

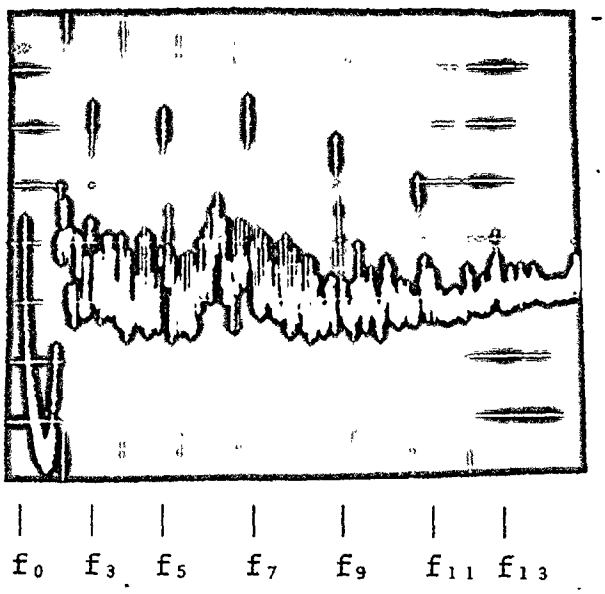

(a) Vertical Scale: 10 dB/div.
Horizontal Scale: 34 MHz/div.

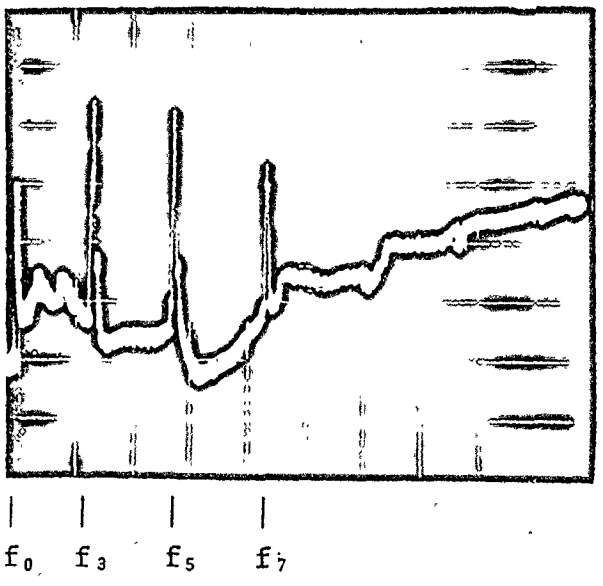

(b) Vertical Scale: 10 dB/div.
Horizontal Scale: 34 MHz/div.

Fig. A.6 (a) Frequency Response of delay line #1 from 0 - 350 MHz.

(b) Frequency Response of delay line #2 from 0 - 350 MHz.

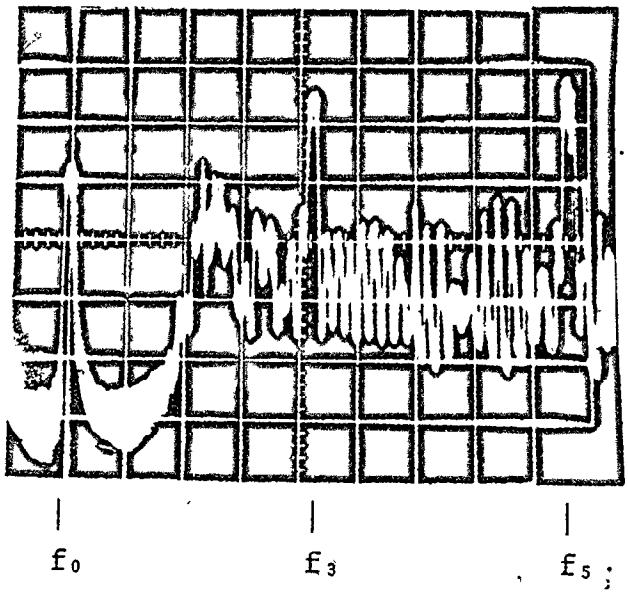

(a) Vertical Scale: 10 dB/div.
Horizontal Scale: 10 MHz/div.

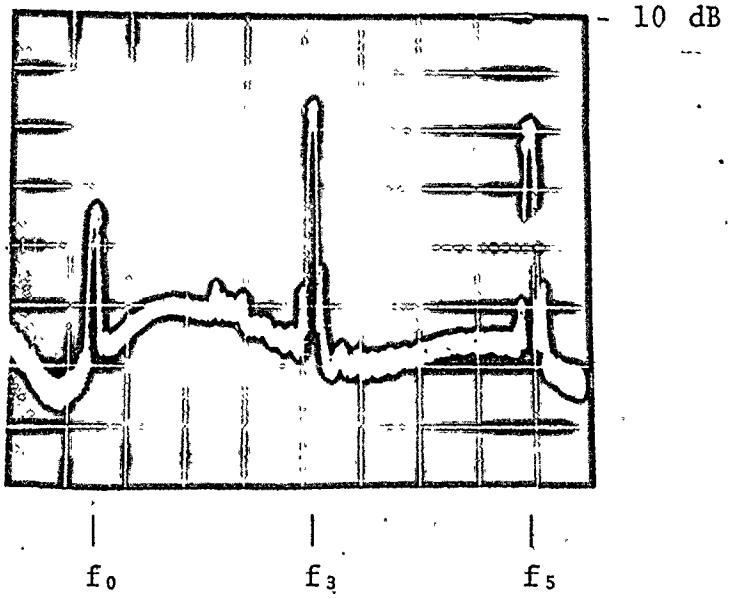

(b) Vertical Scale: 10 dB/div.
Horizontal Scale: 10 MHz/div.

Fig. A.7 (a) Frequency response of delay line #1 in the vicinity of f_3.

(b) Frequency response of delay line #2 in the vicinity of f_3.

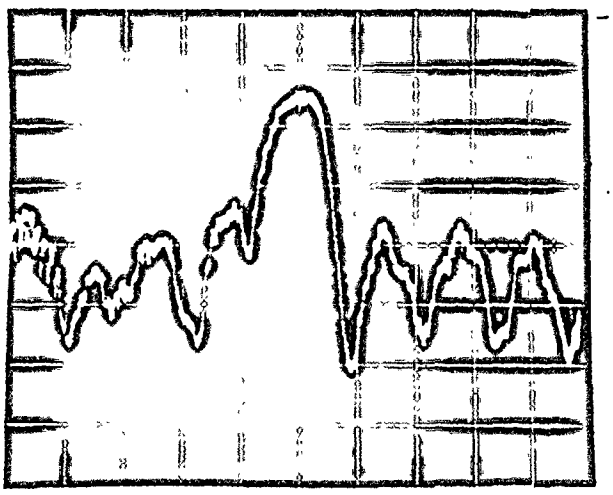

(a) Vertical Scale: 10 dB/div.
Horizontal Scale: 2 MHz/div.

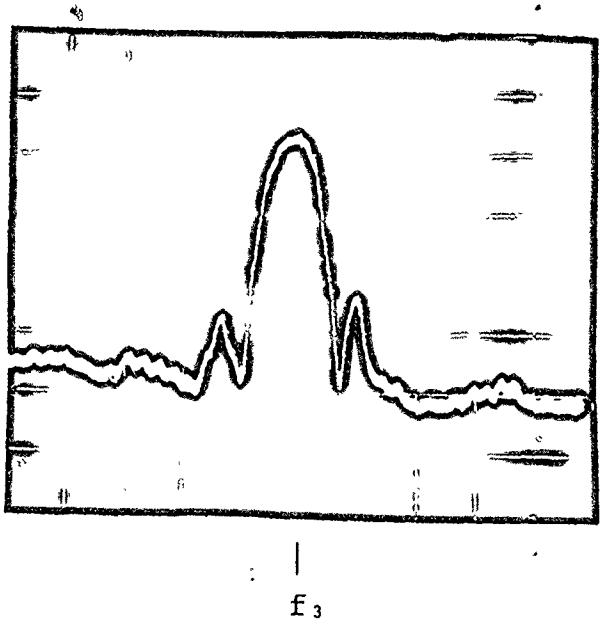

(b) Vertical Scale: 10 dB/div.
Horizontal Scale: 2 MHz/div.

Fig. A.8(a) Frequency response of delay line #1 at f_3.
(b) Frequency response of delay line #2 at f_3.

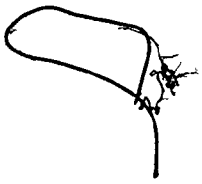

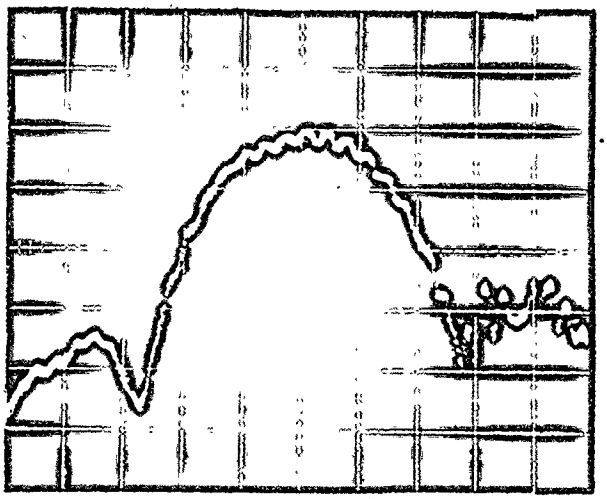

(a) Vertical Scale: 10 dB/div.
Horizontal Scale: 0.5 MHz/div.

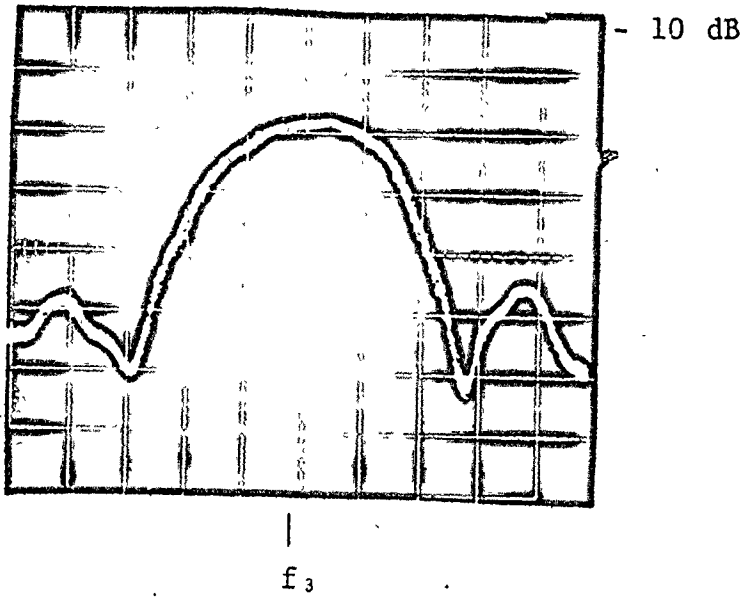

(b) Vertical Scale: 10 dB/div.
Horizontal Scale: 0.5 MHz/div.

Fig. A.9 (a) Pass band of delay line #1 at f_3.
(b) Pass band of delay line #2 at f_3.

transducers at the unused ports (2 and 3) of the MSC, can reduce triple transit reflection.

A.5 Conclusion

The results obtained verified the theory for the excitation of spatial harmonic modes and the isolation of one or more of these modes through the use of the specially designed MSC. The results also show that use of the MSC gives the added benefits of bulk waves, spurious signals and triple transit reflection suppression.

A total isolation of the desired mode was not possible since the other modes were too close (in frequency) to the desired mode, and because the MSC had an inherent wide pass band. Another disadvantage to this method is that for very high frequencies the MSC strip width becomes too small for accurate fabrication.

REFERENCES

1. C. S. HARTMANN, D. T. BELL and R. C. ROSENFELD, "Designing Acoustic Surface Wave Filters", Technical Report, Texas Instruments Advanced Technology Laboratory, TR#-08-73-12, March 1973.
2. W. R. SMITH, Lecture 3 Notes, Massachusetts Institute of Technology, June 18, 1979.
3. R. H. TANCRELL and M. G. HOLLAND, "Acoustic Surface Wave Filters", Proceedings IEEE, 59, March 1971, pp. 393 - 409.
4. H. ENGAN, "Excitation of Elastic Surface Waves by Spatial Harmonics of Interdigital Transducers", IEEE Transactions on Electron Devices, Vol. ED-16, No. 12, Dec. 1969, pp. 1014 - 1017.
5. C. S. HARTMANN, D. T. BELL and R. C. ROSENFELD, "Impulse Model Design of Acoustic Surface-Wave Filters", IEEE Transactions, MTT-21, Apr. 1973, pp. 162 - 175.
6. W. P. MASON, "Electromechanical Transducers and Wave Filters", 2nd Edition, Princeton, N. J. Van Nostrand, 1948.
7. W. R. SMITH, W. F. PEDLER, "Fundamental- and Harmonic-Frequency Circuit-Model Analysis of Interdigital Transducers with Arbitrary Metallization Ratios and Polarity Sequences", IEEE Transactions on Microwave

Theory and Techniques, Vol. MTT-23, No. 11, Nov. 1975, pp. 853 - 864.

8. R. KRIMHOLTZ, "Equivalent Circuits for Transducers Having Arbitrary Asymmetrical Piezoelectric Excitation", IEEE Transactions on Sonics and Ultrasonics, Vol. SU-19, Oct. 1972, pp. 427 - 436.

9. C. K. CAMPBELL, "A Feasibility Study of VHF/UHF Surface Acoustic Wave (SAW) Oscillators", Report to Communications Research Centre, Contract OSU77-00111, McMaster University, Dec. 1977.

10. W. R. SMITH, H. M. GERARD and W. R. JONES, "Analysis and Design of Dispersive Interdigital Surface-Wave Transducers", IEEE Transactions on Microwave Theory and Techniques, Vol. MTT-20, July 1972, pp. 458 - 471.

11. S. J. KERBEL, "Design of Harmonic Surface Acoustic Wave (SAW) Oscillators Without External Filtering and New Data on the Temperature Coefficient of Quartz", Proceedings IEEE Ultrasonics Symposium, 1974, pp. 276 - 281.

12. S. DATTA, B. J. HUNSINGER, "A Generalized Model for Periodic Transducers with Arbitrary Voltages", IEEE Transactions on Sonics and Ultrasonics, Vol. SU-26, May 1979, pp. 235 - 242.

13. C. S. HARTMANN, B. G. SECREST, "End Effects in Interdigital Surface Wave Transducers", Proceedings 1972 IEEE Ultrasonics Symposium, pp. 413 - 416.

14. A. J. BAHR and R. E. LEE, "Equivalent Circuit Model for Interdigital Transducers with Varying Electrode Widths", Electronic Letters, Vol. 9, June 28, 1973, pp. 281 - 282.

15. H. ENGAN, "High-Frequency Operation of Surface-Acoustic-Wave Multielectrode Transducers", Electronic Letters, Vol. 10, 19th Sept. 1974, pp. 395 - 396.

16. F. G. MARSHALL, C. O. NEWTON and E. G. PAIGE, "Theory and Design of the Surface Acoustic Wave Multistrip Coupler", IEEE Transactions on Sonics and Ultrasonics, Vol. SU-20, No. 2, April 1973, pp. 124 - 133.

17. F. G. MARSHALL, C. O. NEWTON and E. G. PAIGE, "Surface Acoustic Wave Multistrip Components and Their Applications", IEEE Transactions on Sonics and Ultrasonics, Vol. SU-20, No. 2, April 1973, pp. 134 - 143.

18. C MAERFIELD, "Multistrip Couplers", Wave Electronics, 2, 1976, pp. 82 - 110.

19. C. MAERFIELD and P. TOURNOIS, "Perturbation Theory for the Surface Wave Multistrip Coupler", Electronic Letters, 9, 1973, pp. 115 - 116.

20. J. TEMMYO and S. YOSHIKAWA, "On the Fabrication and Performance of SAW Delay Line Filters for GHz SAW Oscillators", IEEE Transactions on Sonics and Ultrasonics, Vol. SU-25, No. 6, Nov. 1978, pp. 367 - 371.

21. R. H. TANCRELL, "Analytic Design of Surface Wave Bandpass

Filters", IEEE Transactions on Sonics and Ultrasonics, Vol. SU-21, Jan. 1974, pp. 12 - 22.

22. D. G. SEILER, "Design and Synthesis of a VHF Surface Acoustic Wave Oscillator", M. Eng. Thesis, McMaster University, Dec. 1975.

23. A. J. SLOBODNIK, JR., "VHF and Microwave Frequency Acoustic Surface Wave Delay Lines: Design", Air Force Cambridge Research Laboratories, AFCRL-TR-73-0538, Aug. 1973.

24. H. ENGAN, "Surface Acoustic Wave Multielectrode Transducers", IEEE Transactions on Sonics and Ultrasonics, Vol. SU-22, No. 6, Nov. 1975, pp. 395 - 401.

25. W. R. SMITH, "Basics of the SAW Interdigital Transducer", Wave Electronics, 2 (1976), pp. 25 - 63.

26. J. CRABB, M. F. LEWIS, J. D. MAINES, "Surface Acoustic Wave Oscillators: Mode Selection and Frequency Modulation", Electronic Letters, May 1973, pp. 195 - 197.

27. A. J. BAHR, "Fabrication Techniques for Surface Acoustic Wave Devices", International Specialist Seminar on Component Performance and Systems Applications of Surface Acoustic Wave Devices, Aviemore, Scotland, 23 - 28 Sept. 1973.

28. J. J. CAMPBELL and W. R. JONES, "A Method of Estimating Optimal Crystal Cuts and Propagation Directions for Excitation of Piezoelectric Surface Waves", IEEE Transactions

on Sonics and Ultrasonics, Vol. SU-15, Oct. 1968, pp. 209 - 217.

29. D. G. SEILER AND C. K. CAMPBELL, "Fabrication of Thin Film Interdigital Transducers for Surface Acoustic Wave Devices Operating at Gigahertz Frequencies", Thin Solid Films, 62 (1979), pp. 109 - 114.

30. C. MAERFIELD, P. DEFRANOULD, G. FARNELL, "Some Applications of Non-Symmetrical Multistrip Coupler", 1973 Ultrasonics Symposium Proceedings, pp. 155 - 158.

31. G. W. FARNELL and E. L. ADLER, "An Overview of Acoustic Surface Wave Technology", Final Report to Communications Research Centre on DSS Contract 36001-3-4406.

32. W. R. SMITH, "Key Tradeoffs in SAW Transducer Design and Component Specification", Proceedings 1976 IEEE Ultrasonics Symposium, pp. 547 - 552.

33. K. YAMANOUCHI, F. M. NYFFELER and K. SHIBAYAMA, "Low Insertion Loss Acoustic Surface Wave Filters Using Group-Type Unidirectional Interdigital Transducers", IEEE 1975 Ultrasonics Symposium Proceedings, pp. 317 - 321.